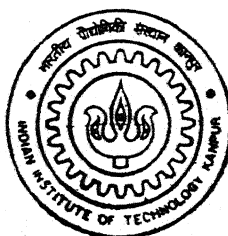


# PHASE UNWRAPPING IN DIGITAL PHOTOELASTICITY BY TILING

by  
ROHIT KUMAR KHODE

TH  
0E/2000/M  
K 528b



DEPARTMENT OF MECHANICAL ENGINEERING  
INDIAN INSTITUTE OF TECHNOLOGY KANPUR

November, 2000

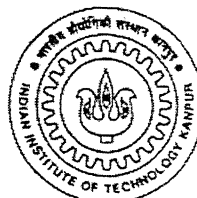
# PHASE UNWRAPPING IN DIGITAL PHOTOELASTICITY BY TILING

A Thesis Submitted  
in Partial Fulfillment of the Requirements  
for the Degree of  
**MASTER OF TECHNOLOGY**

November, 2000

*by*

**ROHIT KUMAR KHODE**



DEPARTMENT OF MECHANICAL ENGINEERING  
INDIAN INSTITUTE OF TECHNOLOGY  
KANPUR – 208016 (INDIA)

## CERTIFICATE

It is certified that the work contained in the thesis entitled, "PHASE UNWRAPPING IN DIGITAL PHOTOELASTICITY BY TILING" by *Mr. Rohit Kumar Khode* has been carried out under my supervision and that this work has not been submitted elsewhere for a degree.



**(Dr. K. Ramesh)**

Professor

Department of Mechanical Engineering,  
Indian Institute of Technology, Kanpur.

November, 2000

133624 / MCE

SEARCHED

INDEXED

133624

SEARCHED

INDEXED

133624



A133624

## ACKOWLEDGEMENTS

I would like to express my deep sense of gratitude and indebtedness towards Dr. K. Ramesh for his inspiring guidance, invaluable suggestions and constructive criticism. He was always a constant source of encouragement throughout my thesis work.

I heartily appreciate the keen interest shown by Dhiraj, Vinayak and Anant in the lab. I would like to thank my *design-2000* friends for making my stay at IITK very enjoyable.

I appreciate the help provided by Mr. Lavendra for conducting the experiments. I express my thanks to ESA laboratory staff for extending their assistance. I thank all those who have contributed directly or indirectly to my thesis.

## ABSTRACT

Photoelasticity is an optical method of experimental stress analysis, which yields a whole field representation of the principal stress difference and its orientation. With advanced digital image processing systems, it has now become possible to get fringe order at every pixel in the domain by the use of phase map generation by interactive approach and phase unwrapping. Though for a large variety of problems phase unwrapping can be applied to whole domain in one step providing only one seed point, certain class of problems having complex geometry need the individual processing of different zones.

The present work discusses the use of tiling for phase unwrapping. The purpose of the present work is to handle the phase map efficiently for correct unwrapping. The various difficulties related to digital implementations are discussed and have been taken care off. Various practical problems having complex geometry are analyzed using completely experimental phase map extracted by six-step phase shifting technique.

A comprehensive software in Windows environment was developed for photoelastic analysis. The software supports fringe order calculation by six step phase shifting algorithm, isoclinic calculation by Brown & Sullivan, Ramesh & Mangal and Patterson & Wang algorithms. Stress separation by conventional Shear Difference and Tesar's Modified techniques is also incorporated.

# CONTENTS

List of Figures.....	I
List of Tables.....	IV
1. INTRODUCTION	
1.1 Introduction.....	1
1.2 Present Work.....	2
1.3 Thesis Layout.....	2
2. OVERVIEW OF DATA AQUISITION TECHNIQUE	
2.1 Introduction.....	4
2.2 Histogram Equalization.....	4
2.3 Thresholding.....	5
2.4 Fringe Thinning	
2.4.1 Global Identification of Fringe Skeleton Based on Intensity Variation.....	6
2.5 Boundary Identification.....	7
2.6 Plane Polariscop	
2.6.1 Intensity of Light Transmitted for a Generic Arrangement of a Plane Polariscop.....	9
2.7 Circular Polariscop	
2.7.1 Intensity of Light Transmitted for a Generic Arrangement of a Circular Polariscop.....	10
2.8 Six-step Phase Shifting Algorithm.....	11
2.9 Evaluation of Isoclinic Parameter	
2.9.2 Algorithm by Ramesh and Mangal.....	16
2.9.2 Algorithm by Brown and Sullivan.....	16
2.10 Closure.....	19

<b>3. PHASE UNWRAPPING BY TILING</b>	
3.1 Introduction.....	20
3.2 Noise Removal in Phase Maps.....	20
3.3 Algorithm for Phase Unwrapping.....	21
3.4 Parameters Affecting Phase Unwrapping	
3.4.2 Influence of Selection of the Phase Unwrapping	
Threshold.....	23
3.4.2 Influence of Location of the Primary Seed Point.....	23
3.5 Use of Tiling Concept for Phase Unwrapping.....	24
3.6 Tiles for Problem of Disk.....	26
3.7 Tiles for Problem of Annular Ring.....	30
3.8 Tiles Applied to Rail Road Contact Problem.....	34
3.9 Tiling for Problem of Spanner and Nut.....	38
3.10 Closure.....	42
<b>4. STRESS SEPARATION USING SHEAR DIFFERENCE TECHNIQUE</b>	
4.1 Introduction.....	43
4.2 Problems in Isoclinic determination.....	43
4.3 Median Filtering in Isoclinic Calculation.....	44
4.4 Shear Difference Technique for Stress Separation	
4.4.1 Conventional Method.....	47
4.4.2 Improvement by Tesar.....	48
4.5 Results and Discussion.....	49
4.6 Closure.....	52
<b>5. CONCLUSION AND SUGGESTIONS FOR FUTURE WORK</b>	
5.1 Conclusion.....	53
5.2 Suggestions for future work.....	53
Reference:.....	55

# LIST OF FIGURES

2.1.	Scheme of logical operators to obtain continuous fringe-skeleton	7
2.2.	Generic arrangement of a plane polariscope	8
2.3.	Generic arrangement of a circular polariscope	10
2.4.	Sequence of six images recorded of a disk under diametral compression for six-step phase shifting algorithm	14
2.5.	Whole field representation of fractional retardation, $\delta_c$ in the form of phase map of a disk under diametral compression obtained with different equations (a-d)	15
2.6.	Sequence of six images recorded of a disk under diametral compression for Ramesh and Mangal algorithm	18
2.7.	Sequence of four images recorded of a disk under diametral compression for Brown and Sullivan algorithm	19
3.1.	Typical phase map for the problem of disk under diametral compression	21
3.2.	Fringe order variation along the horizontal diameter for the problem of disk under diametral compression	22
3.3.	Variation of intensity in phase map of Fig. 3.1 along the vertical diameter	23
3.4.	Tiling for phase unwrapping. Identification of zones for locating the primary seed point: (a) row-wise seeding and column wise scanning (b) column-wise seeding and row-wise scanning. Tiles required for (c) row-wise seeding and column-wise scanning (d) column-wise seeding and row-wise scanning	26
3.5.	(a) Some tiling arrangements for the problem of disk under diametral compression (b),(c) & (d) Tiling arrangements used for unwrapping (e) phase map for problem of disk (f) Sample data points marked on dark field image	27
3.6.	Three dimensional plots for fringe orders unwrapped with different tiling arrangements	29
3.7.	(a) Some tiling arrangements for the problem of ring under diametral compression (b) & (c) Tiling arrangements used for unwrapping (d)	

phase map for problem of ring (e) Sample data points marked on the phase map	31
3.8. Three dimensional fringe orders plots (a) Theoretical data for ring (b), (c) and (d) unwrapped with different tiling arrangements	33
3.9. (a) Some tiling arrangements for the rail road contact problem (b) & (c) Tiling arrangements used for unwrapping (d) phase map for the problem (e) Sample data points marked on the dark field image	35
3.10. Three dimensional fringe order plots for rail road contact problem unwrapped with different tiling arrangements	37
3.11. Tiles for problem of spanner tightening the nut	38
3.12. Improved tiling arrangement for the problem of spanner tightening the nut	39
3.13. Phase map for the spanner problem (a) Obtained with $\cos + \sin$ expression (b) Obtained with interactive approach	39
3.14 (a) Tiles used for unwrapping the phase map of Fig. 3.13b (b) Sample data points shown on the dark field image	41
3.15. Three dimensional fringe order plots for the problem of spanner tightening the nut (a) Unwrapped without tiling (SW isometric) (b) Unwrapped without tiling (NW isometric) (c) Unwrapped with tiles (SW isometric) (d) Unwrapped with tiles (NW isometric)	41
4.1 (a) Isoclinic plot for the problem of disk under diametral compression, obtained by application of Brown and Sullivan algorithm on theoretically simulated images (b) Corresponding theta field	45
4.2. Improved isoclinic data after application of median filter	45
4.3. (a) Isoclinic plot for the problem of disk under diametral compression, obtained by application of Brown and Sullivan algorithm on experimental images (b) Corresponding theta field	46
4.4. (a) Isoclinic plot for the problem of disk under diametral compression, obtained by application of Brown and Sullivan algorithm on low load experimental images (b) Corresponding theta field	46
4.5. Grid needed for applying the shear difference method	47
4.6. Pseudo fringe contours showing variation of stresses, determined using theoretical data by Tesar's Modified Method (a) $\sigma_x$ (b) $\sigma_y$ (c) $\tau_{xy}$	49

4.7. Pseudo fringe contours showing variation of stresses determined using data extracted from theoretically simulated images by Tesar's Modified Method (a) $\sigma_x$ (b) $\sigma_y$ (c) $\tau_{xy}$	50
4.8. Pseudo fringe contours showing variation of stresses determined using data extracted from experimental images by Tesar's Modified Method (a) $\sigma_x$ (b) $\sigma_y$ (c) $\tau_{xy}$	51

## LIST OF TABLES

2.1.	Polariscope arrangement and intensity equations for six-step phase shifting method	12
2.2.	Intensity equations for different orientations of the polarizer and analyzer for Ramesh and Mangal Algorithm	17
2.3.	Polariscope arrangement and intensity equations for polarization stepping schemes (Brown and Sullivan algorithm)	17
3.1.	Unwrapping parameters used for unwrapping complete image for problem of disk	28
3.2.	Unwrapping parameters and tiling plan 1 for problem of disk	28
3.3.	Unwrapping parameters and tiling plan 2 for problem of disk	28
3.4.	Unwrapping parameters and tiling plan 3 for problem of disk	28
3.5.	Fringe orders at some salient points unwrapped with different tiling arrangements	29
3.6.	Unwrapping parameters used for unwrapping complete image for problem of ring	30
3.7.	Unwrapping parameters and tiling plan 1 for problem of ring	30
3.8.	Unwrapping parameters and tiling plan 2 for problem of disk	32
3.9.	Fringe orders at some salient points unwrapped with different tiling arrangements for problem of ring under diametral compression	32
3.10.	Unwrapping parameters used for unwrapping complete image for rail road contact problem	34
3.11.	Unwrapping parameters and tiling plan 1 for rail road contact problem	34
3.12.	Unwrapping parameters and tiling plan 2 for rail road contact problem	36
3.13.	Fringe orders at some salient points unwrapped with different tiling arrangements for rail road contact problem	36
3.14.	Unwrapping parameters used for unwrapping complete image for problem of spanner tightening the nut	40
3.15.	Unwrapping parameters and tiling plan for phase unwrapping of spanner and nut problem	40
3.16.	Fringe orders at some salient points for the spanner and nut problem	



## CHAPTER 1

# INTRODUCTION

### 1.1 Introduction

Photoelasticity deals with the determination of stress fields by the use of polarized light. This method is based on the effect of temporary birefringence. Certain transparent, non-crystalline materials like plexiglass, celluloid, homolite and epoxy are optically isotropic when not loaded but become optically anisotropic and display characteristics similar to crystals when they are stressed. The birefringence in the material is retained only during the application of loads and disappear when they are removed. Measurements of this birefringence provide data, sufficient enough for quantitative determination of the corresponding state of stress. The measurements are made with the help of an optical instrument called polariscope. A polariscope can be used to record maximum shear stress i.e., the difference in the principle stresses and their orientation. Corresponding contours are called isochromatic and isoclinic fringes respectively. The experimentation in photoelasticity involves aquisition of stressed model images at various positions of optical elements, depending on the requirement of a specific algorithm. The main merit of photoelasticity is its simplicity in experimentation as well as in evaluation of stress field.

The main advantage of photoelasticity is that, it can give the stress distribution for the whole field. In conventional methods tedious compensation methods are needed to obtain the fractional fringe order at any point other than the fringe position. Number of data points that could be considered are also less. These procedures are quite involved and requires skill in identification of isochromatics. Hence, automation of data aquisition and analysis to minimize these problems and to provide fast and accurate results has become essential. With advanced digital image processing system, considerable success has been achieved in automating the data aquisition from entire field and it has now become possible to evaluate the total fringe order at every pixel in the domain.

Photoelasticity directly provides only the information of principle stress difference and the direction of the principle stress at the point of interest. Using this, one

can find the normal stress difference and in-plane shear stress by invoking equations in mechanics of solids or Mohr's stress circle. Determination of components of stress tensor requires the use of auxiliary methods.

## 1.2 Present Work

A complete photoelastic analysis in a broad sense can be divided into five major steps,

1. Image aquisition
2. Calibration of model material
3. Retardation calculation
4. Evaluation of isoclinic parameters
5. Stress separation

The software developed so far in the laboratory have remained in text based interface with DOS environment. One of the major thrust of this thesis has been to convert the time tested software to Windows environment.

In digital photoelasticity calibration involves fringe skeletonization, fringe thinning, data collection and analysis of these data in a least squares sense for obtaining the material stress fringe value. Retardation calculation involves two major steps namely, phasemap generation and phase unwrapping. Newer initiatives for phase unwrapping of arbitrary model geometry has been attempted in this thesis. Consideration of arbitrary model geometry requires phase unwrapping in steps and calls for a tiling concept. The algorithms reported by Brown & Sullivan [1] and Ramesh & Mangal [2] (both based on plane polariscope arrangement) are found to give good results [3] for isoclinic determination and are implemented in windows environment in the present work. Finally stress separation using Shear Difference and Tesar's modified technique [4 – 6] are also implemented for the determination of  $\sigma_x$ ,  $\sigma_y$  and  $\tau_{xy}$ .

## 1.3 Thesis Layout

Chapter 2 provides an overview to data aquisition techniques. First histogram equalization and fringe thinning for image enhancement are discussed followed by boundary identification and its representation. Then various algorithms for fringe order and isoclinic determination are briefly discussed.

Parameters affecting phase unwrapping [3] and use of tiling concept for phase unwrapping is discussed in detail in chapter 3. Phase unwrapping for the problems of disc and ring under diametral compression, rail road contact and spanner tightening the nut is discussed in detail.

Chapter 4 discusses the various problems in the evaluation of isoclinic parameter [7]. The use of median filtering for improving the isoclinic result is discussed. Shear difference, Tesar's stress separation techniques and their results for the problem of disk under diametral compression are discussed.

Conclusion and scope for future work is presented in chapter 5.

## CHAPTER 2

# OVERVIEW OF DATA AQUISITION TECHNIQUES

### 2.1 Introduction

Isochromatics and isoclinics are the two fringe contours obtained in a photoelastic experiment. Isochromatic are contours of constant principle stress difference and isoclinics are the loci of points along which the principle stress direction (with respect to the reference axis) is a constant. For stress analysis, the photoelastic data required at any point are,

- The isochromatic fringe order and
- The isoclinic parameter at that point.

The phase shifting technique for photoelastic analysis use direct processing of intensity data for quantitative extraction of isochromatic and isoclinic parameters for every pixel in the domain. Although in certain class of problems it may still be convenient to process a dark or bright field image to collect data of isochromatic fringe order for a few selected points. Generally, the fringes do not appear as thin lines, but they appear as broad bands. So the first step in fringe processing is to identify the actual fringe in this dark band, i.e., fringe skeletonisation.

### 2.2 Histogram Equalization [3]

Histogram equalisation alters the dynamic range and contrast of an image. To perform histogram equalisation, one has to select a function representing a curve to modify the histogram. The available curves include Linear, Bell, Cube, Log and Exponential. This operation has the effect of lightening or darkening an overall image, depending on the curve chosen. The Linear equalisation curve moves the indexes so that the average index density across the grey-scale is even. This equalisation produces high contrast image with the highest possible dynamic range. The Bell equalisation curve moves the indexes in a similar manner, but groups the indexes more closely to the centre of the scale. This equalisation produces a high contrast image but not quite as high a dynamic

range as would be achieved with a linear equalisation curve. The Cube and Log equalisation curves concentrate the range of indexes at the low end of the scale, making the overall image darker. These equalisations produce a high contrast image with a low dynamic range. On the other hand the exponential equalisation curve concentrates the range of indexes at the high end of the scale, making the overall image lighter. The modified image has a high contrast with low dynamic range.

## 2.3 Thresholding [3]

Thresholding is one of the most important technique to image segmentation and is essentially a process of separating background and object modes. The approach is to select a threshold  $T$  that separates these modes. Then, any point  $(x,y)$  for which  $g(x,y) > T$  is called an object point; otherwise the point is called a background point. In a generic sense thresholding may be viewed as an operation that involves test against a function  $T$  of the form,

$$T = f\{x, y, p(x, y), g(x, y)\} \quad (2.1)$$

Where  $g(x,y)$  is the gray level of point  $(x,y)$  and  $p(x,y)$  denotes some local property of these point, for example, the average gray level of a neighborhood centered on  $(x,y)$ . A thresholded image  $b(x,y)$  is defined as,

$$b(x, y) = \begin{cases} 1 & \text{if } g(x, y) > T \\ 0 & \text{if } g(x, y) \leq T \end{cases} \quad (2.2)$$

When  $T$  depends only on  $g(x,y)$ , the threshold is called global. If  $T$  depends on both  $g(x,y)$  and  $p(x,y)$ , the threshold is called local. If, in addition,  $T$  depends on the spatial co-ordinates  $x$  and  $y$ , the threshold is called dynamic.

## 2.4 Fringe Thinning

Due to the nature of formation of fringes, the intensity of pixels in the fringe band (dark/bright) does not remain constant but a variation does exist. Though the variation is not resolvable to a fine degree by a human eye, the present day CCD cameras can easily recognize and quantize it for further processing.

Although the use of intensity information leads to a better approach for fringe thinning, the early methods were confined to treating the fringe field as a binary image. Later, intensity based methods were developed. These techniques can be further classified into mask based methods and global methods. Since the global method is easy to implement and give better results, this was implemented in the software.

#### 2.4.1 Global Identification of Fringe Skeleton Based on Intensity Variation

In general, photoelastic images have high contrast and the edges of the fringes can be extracted easily. Further the use of edge information to identify the fringe skeletons eliminates the occurrence of spurious fringes. Thus in global methods, fringe thinning involves two steps of edge detection and fringe skeletonization.

Edge detection is an important step. The better is the edge detection algorithm; the better will be the skeleton identification [8]. Edge detection by thresholding works very well for photoelastic images. The algorithm is simple and also computationally very fast. If there is intensity variations in the image, one can use either dynamic thresholding or divide the image into convenient segments and use appropriate global threshold for each of the segment to detect fringe edges. The image thus obtained is to be stored in one of the available frame buffers.

The second part of the processing sequence is the skeletonization of the fringes. For this, fringe areas are to be identified first and within the fringe area, the skeleton point needs to be scanned appropriately. One of simplest scanning schemes is row-wise scanning of the image and is applicable for fringes that are vertical or almost vertical. The steps involved are,

1. Scan the thresholded image row-wise from the first pixel to identify the fringe edge.
2. The scanning is carried out from one edge of the fringe to the other edge. Store the gray levels of the pixels within the boundaries of the fringe.
3. Identify the minimum intensity point and mark it as a fringe skeleton pixel.
4. Step (1) and (2) are repeated until all the pixels in the image are scanned and at the end of the process, the thinned image is obtained.

On the other hand, if the scanning is made column-wise, the algorithm can be applied to extract fringe skeletons which are primarily horizontal. To process complex fringe patterns, one requires a more refined scanning method taking into account the curvature and normal of the fringes. Though the idea is conceptually very simple, it is very difficult to implement from software point of view and is also computationally very expensive.

Fringe skeletons that are continuous and free of noise, can be easily extracted by appropriately processing the results of fringe skeletons obtained by a finite number of orthogonal scans. Once the edges are determined, the image is scanned row-wise ( $0^\circ$  scan), diagonal-wise ( $45^\circ$  scan), column-wise ( $90^\circ$  scan) and cross diagonal-wise ( $135^\circ$  scan). Thus at the end of the initial processing, one gets four images of fringe skeletons corresponding to each scan direction. Each of these fringe skeleton is not continuous because of its direction dependence. The use of logical operators as shown in Fig. 2.1 can eliminate this discontinuities and noise [9-10]. The logical “OR” operation between

the orthogonally scanned images helps to get a continuous fringe but the image contains noise. The noise is scan direction dependent and is removed by the logical “AND” operation performed between the logically “OR”ed images.

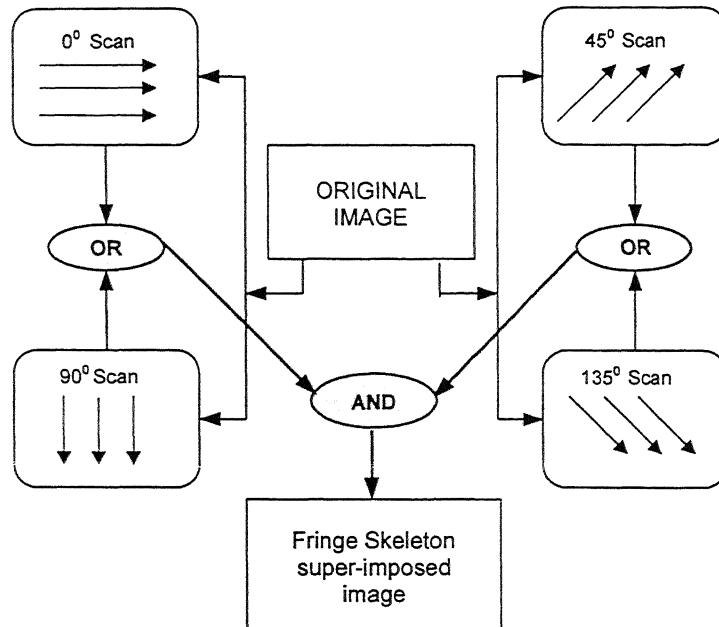


Fig. 2.1. The scheme of logical operators to obtain continuous fringe-skeleton

## 2.5 Boundary Identification

To limit the determination of field parameter within the region of interest (within the specimen), the image has to be segmented. Segmentation of the image is done by detecting the boundary. In DIP literature, boundary of the image is detected using spatial filters like Robert's, Prewitt, Sobel etc. These filters detect the edges based on abrupt change in gray levels. The edge detection algorithms not only detect the boundary, but also detect the regions in the image where there is abrupt change in gray levels. The set of pixels obtained from the above filters seldom characterises a boundary completely. This is because, non-uniform illumination causes breaks in the boundary. In photoelasticity the accurate detection of the boundary is critical to apply algorithms for stress separation. Hence, instead of using the above general edge detection algorithms, the geometric properties of model can be used to detect the boundary accurately. In bright field arrangement of the polariscope, the boundary of the image can be seen clearly. Using this image, the boundary can be detected based on geometric primitives such as line, circle, ellipse and arc etc. The boundary is to be drawn using primitives developed, such that outer side pixels of the line/curve drawn represents the boundary of the specimen. For ease of book keeping it is better to assign a specific gray level to the detected boundary. Once the boundary is identified, to make further computations, the boundary data has to be expressed in a suitable representation. The positions of the

pixels, which have the intensity of 255, are written into two separate intermediate files, one for horizontal scanning (*scanx.dat*) and one for vertical scanning (*scany.dat*). In view of spatial quantization, to represent the segment of the boundary having a curvature, more than one pixel is needed. Further processing of these files are done in which the first and the last column for every line for these files are extracted and stored into two separate files for horizontal scanning (\*.*ybn*) and for vertical scanning (\*.*xbn*).

## 2.6 Plane Polariscope

Plane polariscope is one of the simplest optical arrangement possible. Fig. 2.2 shows the optical arrangement for plane polariscope. A stressed model is kept in the field of view. The incident light on the model is plane polarised. As it passes through the model, the state of polarization changes from point to point depending on the principle stress direction and the magnitude of principle stress difference. The information about the stress field can be obtained if the state of polarization of the emergent light is studied. This is easily achieved by introducing a analyzer at  $0^\circ$ . With the introduction of analyzer, fringe contours that are black appear on the screen. The fringe contours correspond to those points where intensity of light transmitted is zero. Since the analyzer is kept at  $0^\circ$ , this is possible only if the emergent light from the model has its plane of polarization vertical or in other words the incident plane polarized light on the model is unaltered.

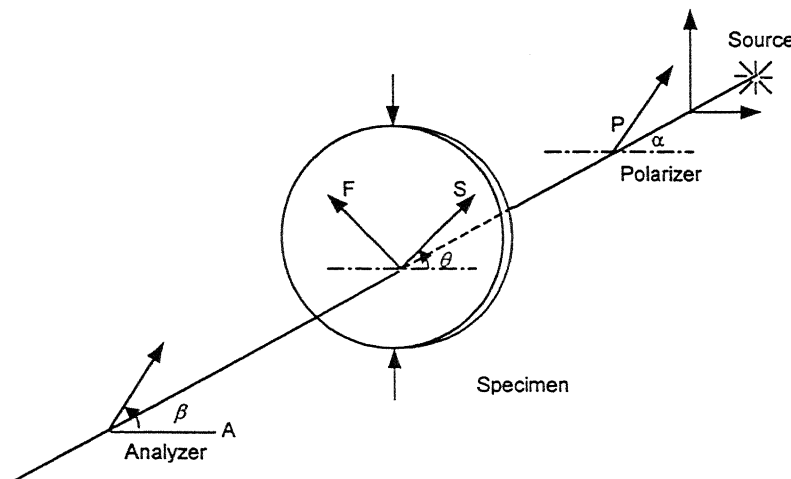


Fig. 2.2 Generic arrangement of a plane polariscope

The incident light is unaltered on all those points where the model behaves like a full wave plate. This happens when the principle stress difference ( $\sigma_1 - \sigma_2$ ) is such as to cause a relative phase difference of  $2m\pi$  ( $m = 0, 1, 2, \dots$ ), where  $m$  is an integer. Since stress is continuous one observes a collection of points forming contours that satisfy the above condition and the respective fringe field is known as *isochromatics*.

Another possibility, wherein the incident light is unaltered is, when the polarizer axis coincides with one of the principle stress directions at the point of interest. In this case, light extinction is not wavelength dependent and one observes a dark fringe even in white light. These are known as *isoclinics* meaning contours of constant inclination. The principle stress direction on all points lying on a isoclinic is a constant.

### 2.6.1 Intensity of Light Transmitted for a Generic Arrangement of a Plane Polariscopic [3]

Figure 2.2 shows a photoelastic specimen kept in a plane polariscope with the polarizer and the analyser kept at arbitrary angles of  $\alpha$  and  $\beta$  respectively. Using Jones calculus, the components of light vector along the analyser axis and perpendicular to the analyser axis are obtained as,

$$\begin{bmatrix} E_\beta \\ E_{\beta+\frac{\pi}{2}} \end{bmatrix} = \begin{bmatrix} \cos \beta & \sin \beta \\ -\sin \beta & \cos \beta \end{bmatrix} \begin{bmatrix} \cos \frac{\delta}{2} - i \sin \frac{\delta}{2} \cos 2\theta & -i \sin \frac{\delta}{2} \sin 2\theta \\ -i \sin \frac{\delta}{2} \sin 2\theta & \cos \frac{\delta}{2} + i \sin \frac{\delta}{2} \cos 2\theta \end{bmatrix} \times \begin{bmatrix} \cos \alpha \\ \sin \alpha \end{bmatrix} k e^{i\alpha x} \quad (2.3)$$

The intensity of light transmitted  $I_p$  (the subscript 'p' denotes that the incident light is plane polarised) is obtained as,

$$I_p = I_a \left[ \cos^2 \frac{\delta}{2} \cos^2(\beta - \alpha) + \sin^2 \frac{\delta}{2} \cos^2(\beta + \alpha - 2\theta) \right] \quad (2.4)$$

where  $I_a$  accounts for the amplitude of incident light vector and the proportionality constant.

### 2.7 Circular Polariscopic

In the case of a circular polariscope, a circularly polarized light is used to reveal the stress information in the model. This is achieved by introducing a quarter wave plate with one of its axis at  $45^\circ$  after the polarizer. The emergent light is analyzed using a combination of quarter wave plate and an analyzer. The basic arrangement is shown in Fig. 2.3. Inside the model boundary, the intensity of light transmitted is governed by the stress field and this can be obtained by Jones calculus.

### 2.7.1 Intensity of Light Transmitted for a Generic Arrangement of a Circular Polariscopic [3]

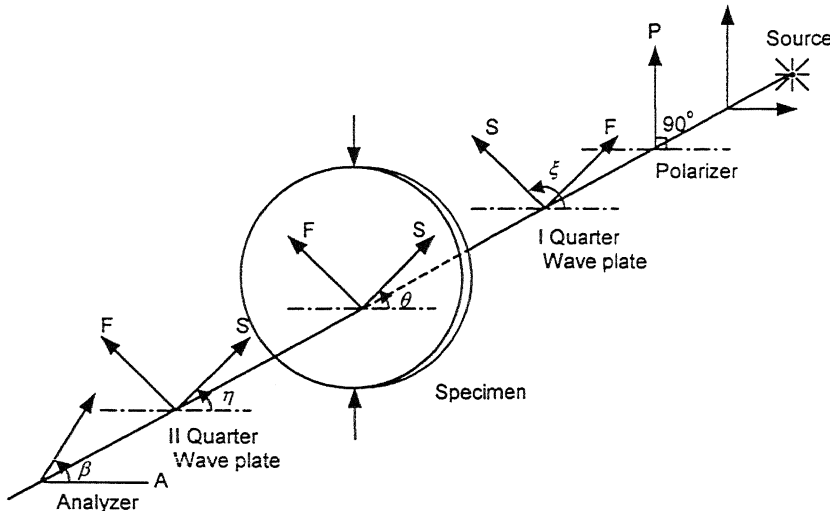


Fig. 2.3. Generic arrangement of a circular polariscopic

Consider the optical arrangement shown in Fig. 2.3 in which the second quarter-wave plate and the analyzer are kept at arbitrary positions. The first quarter-wave plate is kept at  $\xi = 135\text{-deg}$ . Using Jones calculus, the components of light vector along the analyzer axis and perpendicular to the analyzer axis (for  $\xi = 135\text{-deg}$ ) are obtained as,

$$\begin{Bmatrix} E_\beta \\ E_{\beta+\pi/2} \end{Bmatrix} = \frac{1}{2} \begin{bmatrix} \cos \beta & \sin \beta \\ -\sin \beta & \cos \beta \end{bmatrix} \begin{bmatrix} 1 - i \cos 2\eta & -i \sin 2\eta \\ -i \sin 2\eta & 1 + i \cos 2\eta \end{bmatrix} \times \begin{bmatrix} \cos \frac{\delta}{2} - i \sin \frac{\delta}{2} \cos 2\theta & -i \sin \frac{\delta}{2} \sin 2\theta \\ -i \sin \frac{\delta}{2} \sin 2\theta & \cos \frac{\delta}{2} + i \sin \frac{\delta}{2} \cos 2\theta \end{bmatrix} \begin{bmatrix} 1 & i \\ i & 1 \end{bmatrix} \begin{Bmatrix} 0 \\ 1 \end{Bmatrix} k e^{i\omega t} \quad (2.5)$$

The combination of the quarter-wave plate and the polarizer for  $\xi = 135\text{-deg}$  produces a left circularly polarised light. Denoting the intensity of light transmitted as  $I_t$ , the intensity expression is obtained as,

$$I_t = \frac{I_a}{2} + \frac{I_a}{2} [\sin 2(\beta - \eta) \cos \delta - \sin 2(\theta - \eta) \cos 2(\beta - \eta) \sin \delta] \quad (2.6)$$

where  $I_a$  accounts for the amplitude of light vector and proportionality constant. The intensity equation developed show that when the extinction conditions are satisfied, the

intensity of light transmitted should be zero. However, this never happens in an experiment. In order to account for this behaviour a term  $I_b$  is added to account for the stray light/background illumination.

In subsequent discussions, the intensity of light transmitted will be denoted as  $I_i$  for the  $i^{\text{th}}$  optical arrangement. The orientation of the optical element that needs to be rotated will also appear with a subscript  $i$ . Thus, in Eq. (2.6) by adding the term  $I_b$  to account for background illumination/stray light reduce to

$$I_i = I_b + \frac{I_a}{2} + \frac{I_a}{2} [\sin 2(\beta_i - \eta_i) \cos \delta - \sin 2(\theta - \eta_i) \cos 2(\beta_i - \eta_i) \sin \delta] \quad (2.7)$$

## 2.8 Six-step Phase Shifting Algorithm [11]

One of the most successful and time-tested approach of phase shifting to evaluate isoclinic and isochromatic parameter involves the use of six different optical arrangements. The various positions and the respective intensity equations are summarized in Table 2.1. The arrangement shown also accounts for the mismatch of quarter wave plate error.

Using the intensity equation listed in Table 2.1, the isoclinic parameter  $\theta$  is obtained as,

$$\theta_c = \frac{1}{2} \tan^{-1} \left( \frac{I_5 - I_3}{I_4 - I_6} \right) \quad (2.8)$$

From the equations shown in Table 2.1, the fractional retardation  $\delta$  is obtained as,

$$\delta_c = \tan^{-1} \left( \frac{(I_4 - I_6)}{(I_1 - I_2) \cos 2\theta_c} \right) = \frac{1}{2} \tan^{-1} \left( \frac{I_a \cos 2\theta_c \sin \delta_c}{I_a \cos 2\theta_c \cos \delta_c} \right) \quad (2.9)$$

$$\delta_c = \tan^{-1} \left( \frac{(I_5 - I_3)}{(I_1 - I_2) \sin 2\theta_c} \right) = \frac{1}{2} \tan^{-1} \left( \frac{I_a \sin 2\theta_c \sin \delta_c}{I_a \sin 2\theta_c \cos \delta_c} \right) \quad (2.10)$$

In Eqs. (2.8) to (2.10) the subscript ‘ $c$ ’ for the  $\theta$  or  $\delta$  indicates that the principal values of the inverse trigonometric function is referred. In subsequent discussion too the same symbolism will be used.

It is clear that the exact calculation of isoclinic angle and fractional retardation is not trivial from Eqs. (2.8) to (2.10). Equation (2.8) shows that the isoclinic value is indeterminate at those points where  $\delta_c = 0, \pi, 2\pi, 3\pi, \dots$ . The implication is that the isoclinic contour will not be continuous over the domain. When  $\delta_c$  is not exactly equal to 0 or  $\pi$  or  $2\pi$  etc. but very close to these values,  $\theta_c$  does not become indeterminate but the value of  $\theta_c$  determined will be unreliable and appears as noise in isoclinic fringe when plotted. This is known as isochromatic-isoclinic interaction in the calculation of the isoclinic parameter.

**Table 2.1.** Polariscope arrangement and intensity equations for six-step phase shifting method.

$\xi$	$\eta$	$\beta$	Intensity equation
$3\pi/4$	0	$\pi/4$	$I_1 = I_b + \frac{I_a}{2}(1 + \cos \delta)$
$3\pi/4$	0	$3\pi/4$	$I_2 = I_b + \frac{I_a}{2}(1 - \cos \delta)$
$3\pi/4$	0	0	$I_3 = I_b + \frac{I_a}{2}(1 - \sin 2\theta \sin \delta)$
$3\pi/4$	$\pi/4$	$\pi/4$	$I_4 = I_b + \frac{I_a}{2}(1 + \cos 2\theta \sin \delta)$
$\pi/4$	0	0	$I_5 = I_b + \frac{I_a}{2}(1 + \sin 2\theta \sin \delta)$
$\pi/4$	$3\pi/4$	$\pi/4$	$I_6 = I_b + \frac{I_a}{2}(1 - \cos 2\theta \sin \delta)$

Considering that  $\theta_c$  is calculated correctly by Eq. (2.8), the calculation of  $\delta_c$  by Eqs. (2.9) or (2.10) should result in the same value of  $\delta_c$  if continuous variables are used in the arctangent calculations. In practical applications, this is not the case due to intensity digitisation and quantization and only discrete values are used in the arctangent calculations. This can lead to error in the calculations. Further, in Eqs. (2.9) and (2.10),  $\delta_c$  has low-modulation regions when  $\cos 2\theta_c$  or  $\sin 2\theta_c$  are small. In these regions, the intensity differences  $(I_4 - I_6)$  or  $(I_5 - I_3)$  will also be small. The evaluation of  $\delta_c$  will involve the ratio of two small discrete numbers and will be in considerable error in such regions. This is termed as isoclinic-isochromatic interaction in the calculation of the fractional retardation. Apart from this, the principal value of  $\theta_c$  evaluated by Eq. (2.8) lies in the range  $-\pi/4$  to  $\pi/4$  and an ambiguity exists on whether  $\theta_c$  corresponds to  $\sigma_1$  or  $\sigma_2$  direction over the domain.

It is instructive to note that regions of low values of  $\cos 2\theta_c$  coincide with high values of  $\sin 2\theta_c$  and vice versa. Therefore for every point in the region of interest one has two estimates of  $\delta_c$  with different degrees of error depending on the region. Thus, the results must be combined appropriately to get the best possible values of  $\delta_c$ . For the whole domain it is obtained as,

$$\delta_c = \tan^{-1} \left( \frac{(I_5 - I_3) \sin 2\theta_c + (I_4 - I_6) \cos 2\theta_c}{(I_1 - I_2)} \right) = \tan^{-1} \left( \frac{I_a \sin \delta_c}{I_a \cos \delta_c} \right) \quad (2.11)$$

Unlike Eqs. (2.9) or (2.10), Eq. (2.11) always guarantees a high modulation over the field [12].

Figure 2.4 shows the sequence of six images recorded for a disk under diametral compression (dia 60.10 mm, thickness 6.28 mm and load 773.0 N). The material stress fringe value is calculated by digital technique and is found to be 11.9973 N/mm/fr. Figure 2.5a shows the phase map obtained by Eq. (2.11). on scrutiny one can see that near the load application points the phase map is not good. This is not just due to high stress gradient but is due to the interaction of isoclinic on the isochromatic evaluation. The principal values of  $\theta_c$  of Eq. (2.8) lies in the region  $-\pi/4 \leq \theta_c \leq \pi/4$  whereas, physically, principal stress direction lies in the range  $-\pi/2 \leq \theta \leq \pi/2$  and this introduces an ambiguity on  $\delta$  evaluation. Figure 2.5b shows the phase map obtained from experimental images using the theoretically calculated  $\theta$  indicating the  $\sigma_1$  direction throughout the domain. The phase map is uniformly good over the domain.

Though, phase shifting can provide  $\delta$  over the whole domain, certain level of human interaction is needed to correctly identify its sign for unwrapping. This is one of the serious limitation of the technique and could be resolved only when isoclinic is unwrapped correctly over the domain corresponding to either  $\sigma_1$  or  $\sigma_2$  direction uniformly over the domain. This problem is current area of research and automatic solution is still elusive. Figure 2.5c shows the phase map of 2.5a improved by the interactive approach developed by Ramesh and Mangal [13]. The approach is general one and is applicable for any problem and one requires the information of fringe gradient in the bad zone for phase map improvement. Figure 2.5d shows another way of phase map improvement which is specific to the problem of circular disc under diametral compression by unwrapping the  $\theta_c$  in the following manner. In the first and third quadrant ,

$$\theta = \begin{cases} \theta_c & \text{if } (\theta \geq 0) \\ \theta_c + \pi/2 & \text{if } (\theta < 0) \end{cases} \quad (2.12)$$

and in the second and fourth quadrant ,

$$\theta = \begin{cases} \theta_c & \text{if } (\theta < 0) \\ \theta_c - \pi/2 & \text{if } (\theta \geq 0) \end{cases} \quad (2.13)$$

The basic advantage of phase shifting is that inverse tangent functions are used for  $\delta$  calculation. The unwrapping of  $\delta$  becomes a lot more simpler and straight forward.

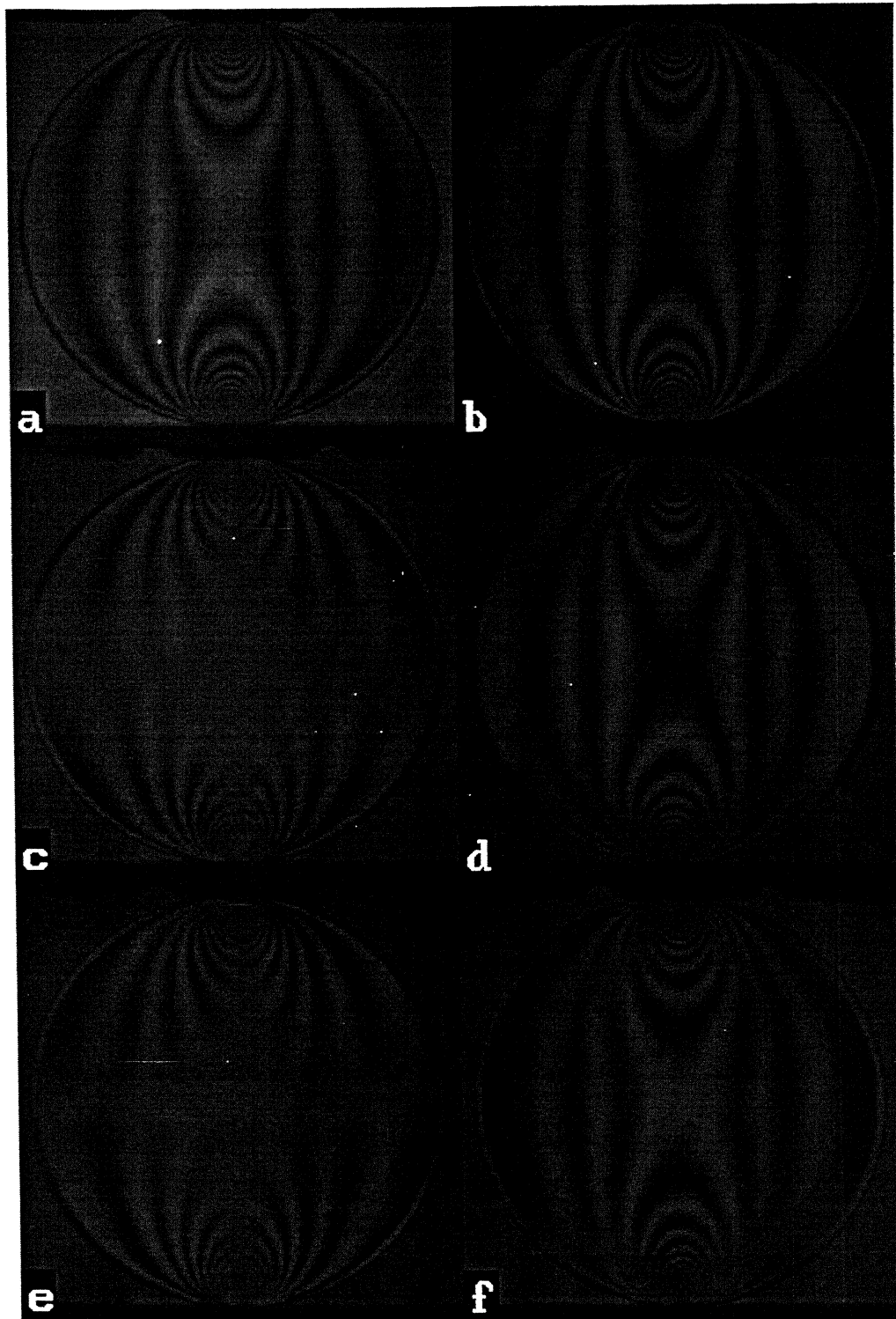


Fig. 2.4. Sequence of six images recorded of a disk under diametral compression (dia 60.10 mm, thickness 6.28 mm and load 773.0 N) for the optical position listed in Table 2.1

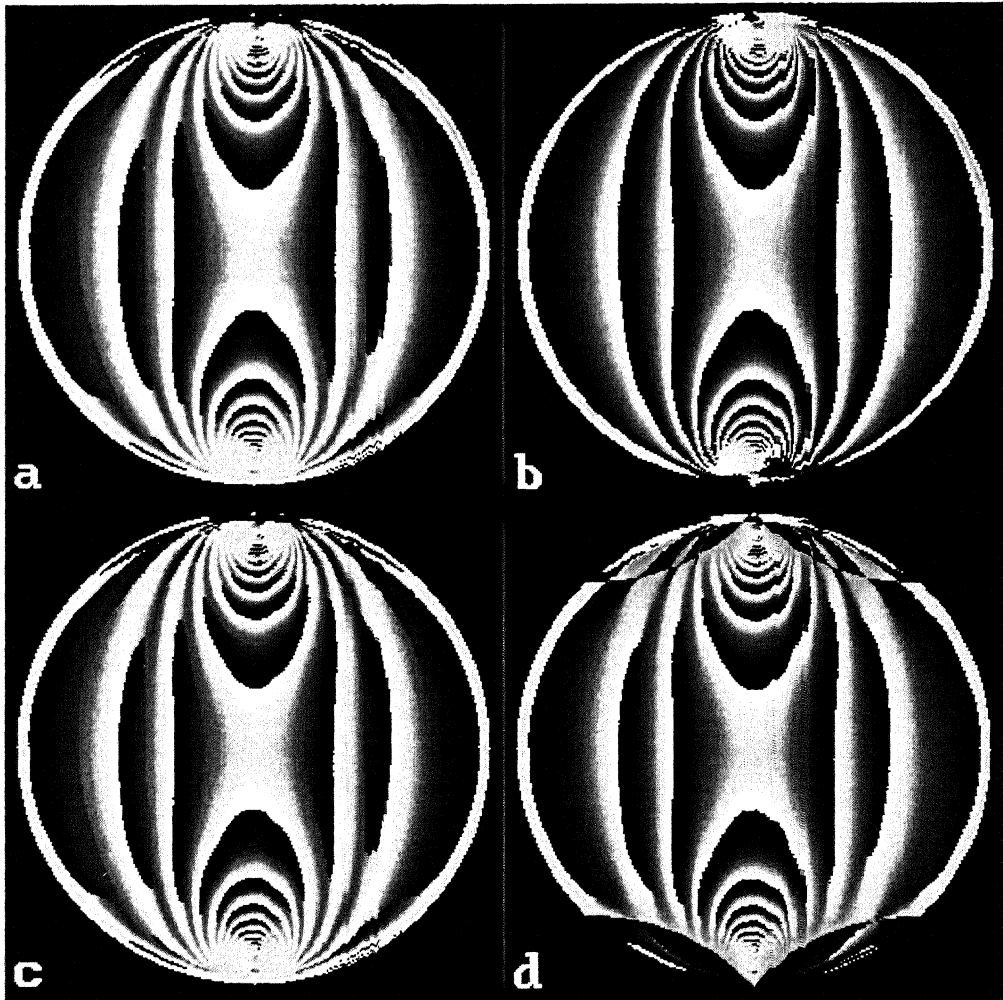


Fig. 2.5. Whole field representation of fractional retardation,  $\delta_c$  in the form of phase map of a disk under diametral compression obtained using Eq.(2.11) with  $\theta_c$  being calculated by various means: **a**  $\theta_c$  by Eq. (2.8) and  $\delta_c$  by Eq. (2.11) **b**  $\theta_c$  by theory corresponding to the  $\sigma_1$  direction and  $\delta_c$  by Eq. (2.11) **c** phase map Fig. 2.3a improved by interactive approach **d**  $\theta_c$  by Eq. (2.8) then unwrapped by Eqs. (2.12) & (2.13) according to quadrant and  $\delta_c$  by Eq. (2.11)

## 2.9 Evaluation of isoclinic parameters

There are a number of algorithms available for isoclinic angle calculation based on either circular or plane polariscope arrangement. The algorithm in plane polariscope arrangement are,

- Ramesh and Mangal [2]
- Brown and Sullivan [1]
- Chen and Lin [14]
- Dupre et al. [15]
- Sarma et al. [16]
- Kihara [17]

Of these, the methods of Brown & Sullivan and Chen & Lin are actually called as polarization stepping methods while the remaining methods are called as phase shifting methods.

Out of these algorithms, the algorithm given by Ramesh & Mangal and Brown & Sullivan are found to give good results [7] and are implemented in windows environment.

### 2.9.1 Algorithm by Ramesh and Mangal [2]

In this, the polarizer and analyzer are kept at arbitrary positions. The intensity of light transmitted is given by Eq. (2.4). If the term  $I_b$  is added to account for stray light/background illumination, one gets

$$I_i = I_b + I_a \left[ \sin^2 \beta_i \cos^2 \frac{\delta}{2} + \sin^2 \frac{\delta}{2} \sin^2 (2\theta - \beta_i) \right] \quad (2.14)$$

If one takes all possible combinations of  $\alpha$  and  $\beta$  in steps of  $\pi/4$ , then only six intensity equations turn out to be unique which are given in Table 2.2. Out of these only the first four intensity equations, the isoclinic parameter is calculated as,

$$\theta_c = \frac{1}{4} \tan^{-1} \left( \frac{I_3 - I_2}{I_4 - I_1} \right) = \frac{1}{4} \tan^{-1} \left( \frac{I_a \sin^2 \frac{\delta}{2} \sin 4\theta}{I_a \sin^2 \frac{\delta}{2} \cos 4\theta} \right) \text{ for } \sin^2 \frac{\delta}{2} \neq 0 \quad (2.15)$$

Use of atan2 function is recommended for evaluating  $\theta_c$  from Eq. (2.15). Figure 2.6 shows the experimentally recorded images for the disk.

### 2.9.2 Algorithm by Brown and Sullivan [1]

In this polarizer and analyzer are kept crossed and four images are obtained at step of  $\pi/8$  radians. The polarisation steps used by Brown and Sullivan and the appropriate intensity equations are summarised in Table 2.3. Figure 2.7 shows the experimentally recorded images for the ring. Isoclinic parameter is calculated as,

$$\theta_c = \frac{1}{4} \tan^{-1} \left( \frac{I_4 - I_2}{I_3 - I_1} \right) = \frac{1}{4} \tan^{-1} \left( \frac{I_a \sin^2 \frac{\delta}{2} \sin 4\theta}{I_a \sin^2 \frac{\delta}{2} \cos 4\theta} \right) \text{ for } \sin^2 \frac{\delta}{2} \neq 0 \quad (2.16)$$

Use of atan2() function is recommended for evaluating above equation.

**Table 2.2.** Table showing the intensity equations for different orientations of the polarizer and analyzer

Ramesh and Mangal Algorithm

$\alpha$	$\beta$	Intensity equation
0	$\pi/2$	$I_1 = I_b + I_a \sin^2 \frac{\delta}{2} \sin^2 2\theta$
$\pi/4$	$\pi/2$	$I_2 = I_b + \frac{I_a}{2} \left[ 1 - \sin^2 \frac{\delta}{2} \sin 4\theta \right]$
0	$\pi/4$	$I_3 = I_b + \frac{I_a}{2} \left[ 1 + \sin^2 \frac{\delta}{2} \sin 4\theta \right]$
$\pi/4$	$3\pi/4$	$I_4 = I_b + I_a \sin^2 \frac{\delta}{2} \cos^2 2\theta$
$\pi/4$	$\pi/2$	$I_5 = I_b + I_a \left[ \cos^2 \frac{\delta}{2} + \sin^2 \frac{\delta}{2} \sin^2 2\theta \right]$
0	0	$I_6 = I_b + I_a \left[ \cos^2 \frac{\delta}{2} + \sin^2 \frac{\delta}{2} \cos^2 2\theta \right]$

**Table 2.3.** Polariscope arrangements and intensity equations for polarization stepping schemes.Brown and Sullivan (Polarizer & Analyzer crossed;  $\alpha = \beta + \pi/2$ )

$\alpha$	Intensity equation
0	$I_1 = I_b + I_a \sin^2 \frac{\delta}{2} \sin^2 2\theta$
$\pi/8$	$I_2 = I_b + \frac{I_a}{2} \sin^2 \frac{\delta}{2} (1 - \sin 4\theta)$
$\pi/4$	$I_3 = I_b + I_a \sin^2 \frac{\delta}{2} \cos^2 2\theta$
$3\pi/8$	$I_4 = I_b + \frac{I_a}{2} \sin^2 \frac{\delta}{2} (1 + \sin 4\theta)$

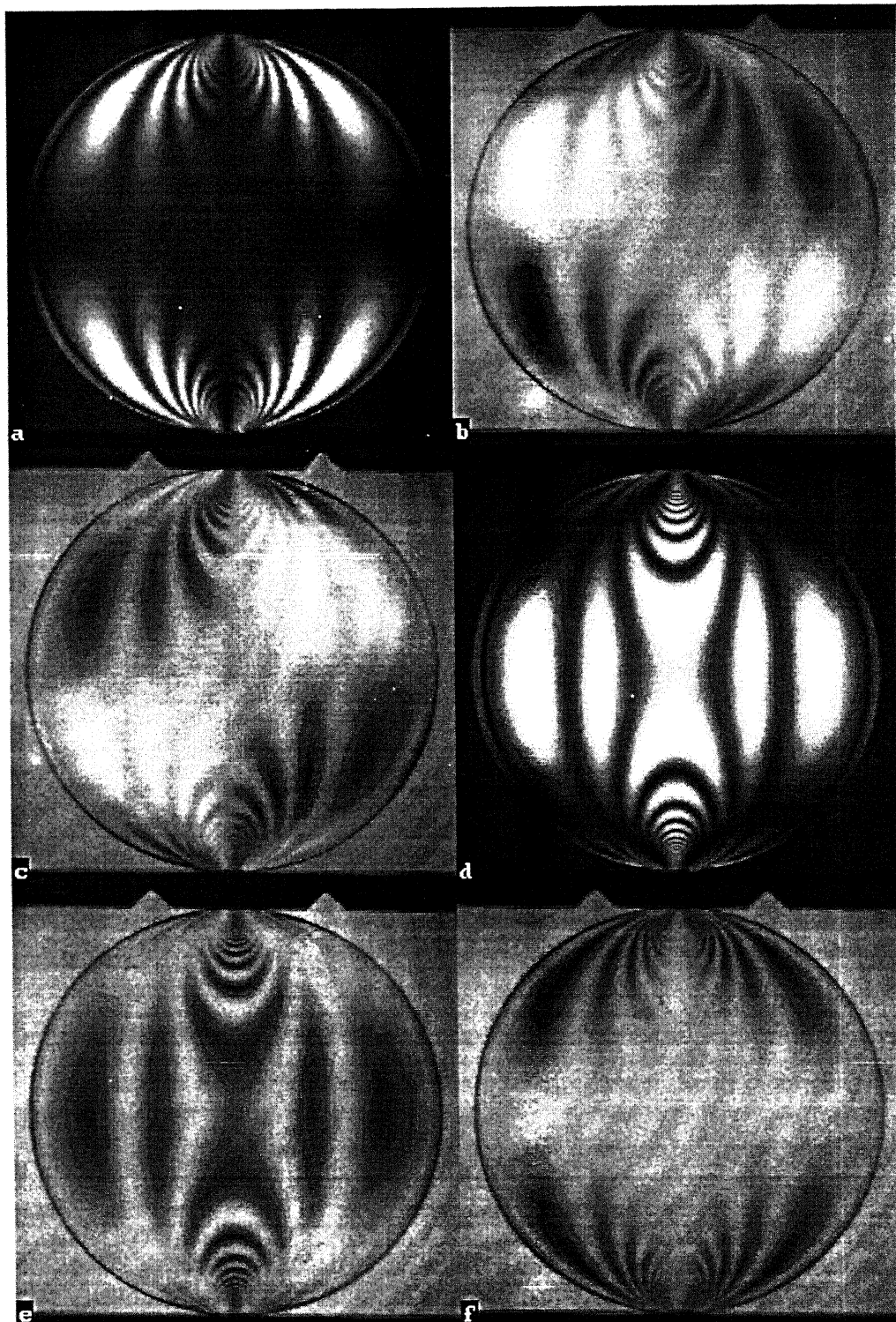


Fig. 2.6. Sequence of six images recorded of a disk under diametral compression for the optical position listed in Table 2.2

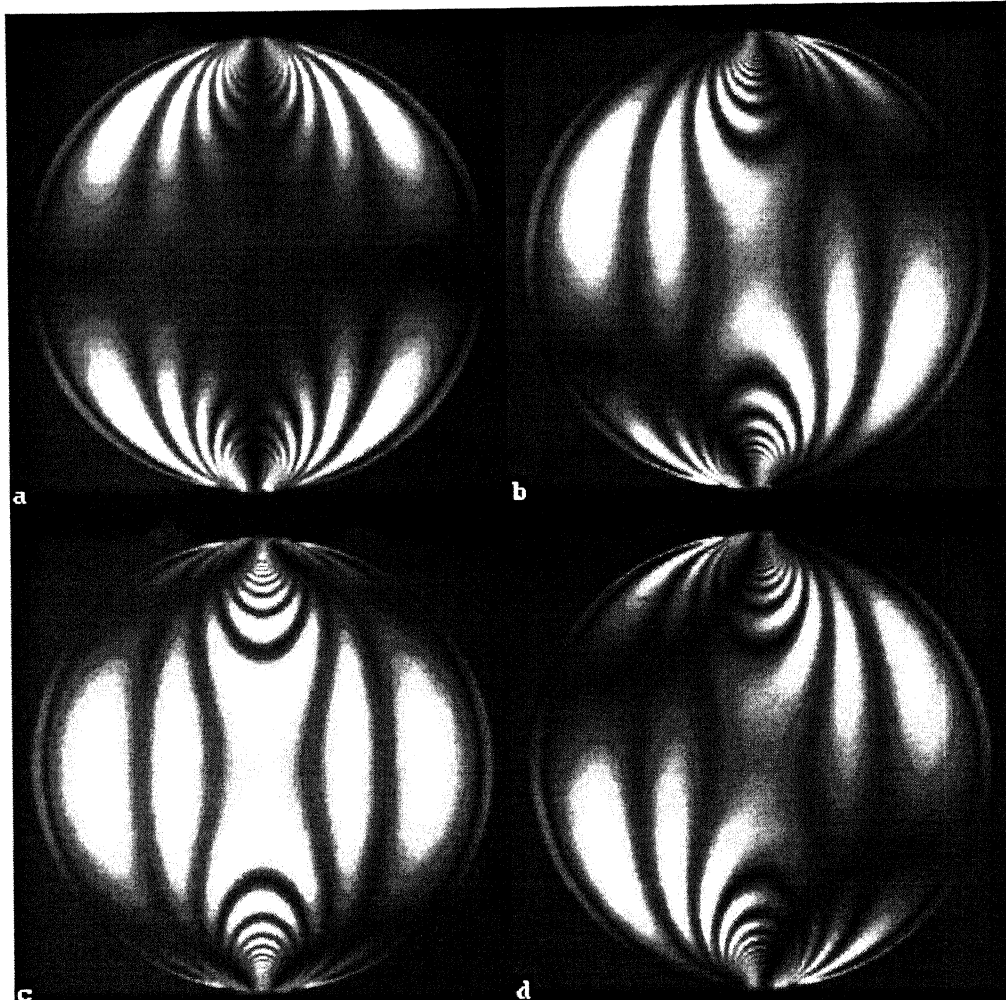


Fig. 2.7. Sequence of four images recorded of a disk under diametral compression for the optical position listed in Table 2.3

## 2.10 Closure

An overview to data aquisition techniques was presented in this chapter. Histogram equalization and fringe thinning algorithm are presented. Six step phase shifting algorithm for isochromatic determination was discussed. Algorithms reported by Ramesh & Mangal and Brown and Sullivan for isoclinic determination were discussed in brief.

## PHASE UNWRAPPING BY TILING

### 3.1 Introduction

In the previous chapter, six-step phase shifting algorithm to obtain fractional retardation over the complete model domain has been presented. In this technique, the fractional retardation is represented as a phase map. In the phase map, the fractional fringe orders in the range of 0-1 are represented as an intensity map of 0-255 gray level. For practical utilization of the data, one has to find the total fringe order over the domain. This is achieved by a process called phase unwrapping. For phase unwrapping to be effective, phase map should be free of noise and discontinuities.

Though the algorithm for phase unwrapping is simple and straight forward, there are certain practical problems that affect phase unwrapping. Selection of threshold gray level  $T_p$ , for unwrapping and location of primary seed point are two major parameters that affect the phase unwrapping process [3].

Problems emerging from choice of primary seed point can be overcome by the use of tiling concept, and is discussed in detail in this chapter. With the use of tiling, the area of phase map containing noise can be treated separately and propagation of error due to noise can be avoided.

### 3.2 Noise Removal in Phase Maps

The phase maps in general may have *salt and pepper noise* (binary noise) at a few points in the domain. To remove noise from images which have sharp edges, usually a median filter is used as other filters can destroy the sharp edges. The median filter is a non-linear spatial filter. In this, the grey level of each pixel is replaced with the median of the grey levels in the neighbourhood of that pixel. Even though, the median filter preserves the sharp edges, some information at the sharp edges is lost. The intensity gradient at the transition of wrapped regions is the main parameter for unwrapping of the phase. Any decrease in the intensity at the transition regions will affect phase unwrapping adversely. Thus, median filter is not an ideal choice for the present application. For removing the noise without disturbing the sharp edges, the following noise removal algorithm can be used.

This algorithm removes the binary noise based on the difference in the intensities between the neighbourhood pixels along the scanning direction. If the difference in intensities between the current pixel and the neighbourhood pixels along the scanning direction is beyond a threshold, then the current pixel is identified as a noise pixel. The grey level of this pixel is replaced with the average of grey levels of the neighbourhood pixels.

Let the noise removal gradient threshold be  $T_n$ . Scanning the image horizontally, the pixel at  $(0, 0)$  is a salt noise pixel when the following condition is satisfied.

$$(g_{00} - g_{-10}) > T_n \quad \text{and} \quad (g_{10} - g_{00}) < -T_n \quad (3.1)$$

The pixel at  $g(0,0)$  has pepper noise when the following condition is satisfied.

$$(g_{00} - g_{-10}) > -T_n \quad \text{and} \quad (g_{10} - g_{00}) < T_n \quad (3.2)$$

The grey level of the noise pixel  $g(0, 0)$  is then replaced with the grey levels of the neighbourhood pixels  $[(g_{-10} + g_{10})/2]$ . In practice, the noise removal scheme could be merged with the program doing fractional retardation calculation itself.

The value of  $T_n$  depends on the maximum grey level gradient between the neighbourhood pixels in the data region and one has to select it by trial and error.

### 3.3 Algorithm for Phase Unwrapping [3]

Figure 3.1 shows the phase map for the case of a disk under diametral compression. The variation of intensity in the phase map along the horizontal diameter is shown in Fig. 3.2. It can be seen that the fractional fringe order increases in the direction in which total fringe order increases and a discontinuity in the slope occurs when the phase retardation is  $2\pi$ .

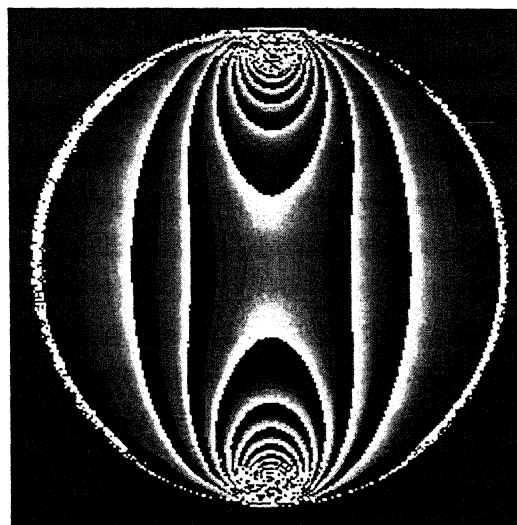


**Fig. 3.1.** Typical phase map for the problem of disk under diametral compression

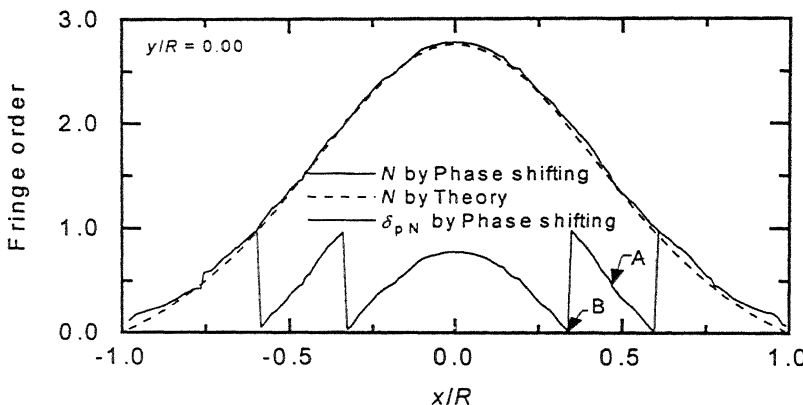


Fig. 3.2. Fringe order variation along the horizontal diameter for the problem of disk under diametral compression

If an integer fringe order is added or subtracted at the transition of the wrapped regions, the total fringe order can be known. The slope of the curve can decide addition or subtraction. If it is positive, then, one has to add the integer value, otherwise subtract. The methodology however requires the total fringe order for at least one point in the domain to be supplied by auxiliary means. The point at which total fringe order is interactively supplied is termed as *primary seed point*.

To unwrap the phase completely within the boundary, the image has to be scanned completely. A simple procedure is to scan the image along the row passing through the primary seed point followed by column-wise scanning of the entire image. The initial scanning along the row provides seed points for effecting the scanning along the columns. These seed points are termed as *secondary seed points*. The entire scheme can be termed as row-wise seeding and column-wise scanning.

Let point 'A' in Fig. 3.2 be the primary seed point at which the total fringe order is to be supplied externally. Once the point is selected the software asks for unwrapping threshold  $T_p$  and total fringe order at that point. The unwrapping is first done along the left direction and then along the right direction. At point 'B' there is a discontinuity in the slope. This discontinuity in the slope is identified by the threshold value  $T_p$ . When the slope between the neighborhood pixels is less than  $-T_p$ , the total fringe order is increased by one and when the slope between neighborhood pixels is greater than  $T_p$ , the total fringe order is decreased by one.

Though in principle the fractional fringe order gradually increases in the direction of the overall fringe gradient, there can be kinks in the curve, due to random noise, which escaped the noise removal procedure. Since phase unwrapping is basically a scanning procedure, this noise can easily propagate and will adversely affect the final results unless corrective measures are taken. Every effort must be made to select the primary seed point such that, no noise is present in the row containing primary seed point.

The other scanning algorithm first generates secondary seed points in the column containing primary seed point followed by row-wise scanning. This is called column-wise seeding and row-wise scanning.

### 3.4 Parameters Affecting Phase Unwrapping

#### 3.4.1 Influence of the Selection of the Phase Unwrapping Threshold [3]

Unwrapping threshold  $T_p$  identifies the transition regions of phase map. In analog data processing one can take  $T_p$  as 255. However, in digital data processing even in small stress gradient zones, one has to take a smaller value of  $T_p$  than 255 to accommodate the effect of spatial discretization and intensity quantization. This aspect is prominent in high stress gradient zones. Variation of the intensity in phase map along vertical diameter for the problem of circular disc under diametral compression is shown in Fig. 3.3. It can be observed, that, at stress concentration regions, the intensity in the wrapped regions neither starts with a value of 0 nor ends with a value of 255. This is primarily due to the fact that the fringe gradient is so high that one requires sub-pixel calculations to identify the exact transition zone.

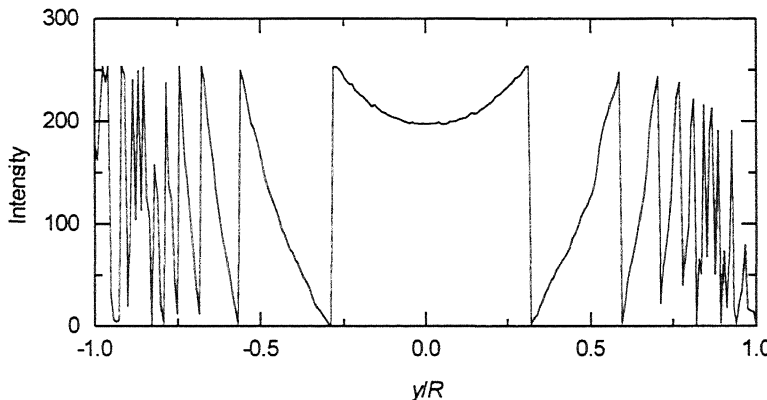


Fig. 3.3. Variation of intensity in phase map of Fig. 3.1 along the vertical diameter

The error in mismatch of quarter-wave plates also plays a role in deciding the value of  $T_p$ . Error in mismatch of quarter-wave plates has the effect of slightly shifting the point of transition and the intensity does not reach the maximum value of 255 [18].

From the above discussion it is clear that  $T_p$  should be lower than 255. In general,  $T_p$  should be higher than the threshold,  $T_n$  that is used to identify noise in the domain.

#### 3.4.2 Influence of the Location of the Primary Seed Point [3]

To initiate the phase unwrapping procedure, the user has to specify the total fringe order for at least one point in the field. Ideally, the location of this point should be arbitrary and the phase unwrapping procedure should be flexible enough to unwrap the phase for

the entire domain. However, the phase unwrapping algorithm could be a lot simpler if the user selects the primary seed point appropriately. The choice of location of seed point depends largely on the specific geometry of the specimen under consideration.

For example, for the problem of disk under diametral compression, while using the row-wise seeding and column-wise scanning scheme to unwrap the entire image, the primary seed point should be chosen along the horizontal diameter. If not, the secondary seed points will be generated only up to the boundary, that is encountered along the row-wise seeding. On the other hand, if column-wise seeding and row-wise scanning is used, the primary seed point must lie on the vertical diameter. In general, the primary seed point should be located on a horizontal line covering the entire width of the model, if row-wise seeding and column wise scanning is used and vice versa.

This problem is further enhanced if the model geometry is complex. For example, for the problem of annular ring under diametral compression, where no single primary seed point can be specified which will efficiently unwrap the phase map. In this case, if true boundary information is used then there will always be limited seeding. Otherwise, if only outer boundary information is used, for all points inside the inner boundary, the secondary seed points generated will not have any significant secondary seed value, as phase map itself contains noise in that zone. This problem of limited unwrapping and insignificant seeding can be overcome by adopting a tiling procedure for phase unwrapping.

### 3.5 Use of Tiling Concept for Phase Unwrapping

Tiling in a broad sense can be understood as, treating the whole image as an assembly of small windows called tiles. The process parameters can individually be selected for each of the tiles and processed information of each tile can then be reassembled to obtain the final results (or overall image) as if the whole image was processed simultaneously. In image processing, such operations are mostly used for intensity manipulations and can be easily accomplished by using the frame buffer memory. However, in case of phase unwrapping this approach is not possible as unwrapped fringe orders are *real numbers*, that can't be stored in pixel locations of a frame buffer. For storing the fringe order values, a file structure has to be used. This poses certain restrictions on the selection of the nature of the tiles. Selecting an arbitrary window would be difficult from book keeping point of view. Even if an efficient file structure is used, pasting of processed information back to the original place from each of the file is a difficult process and will require tedious programming efforts. This restricts the shape of tiles either as vertical strips filling the entire height of the image or as horizontal strips filling entire width of the image.

An alternative approach is to declare a large matrix of real numbers, which is equal to size of the image. In such case any arbitrary window can be selected. Though this is not a feasible approach on the systems having small RAM size, but for present day systems with RAM size exceeding that of 64 Mb, this approach is quite useful and efficient. Also maintaining a file structure, as required in first approach is logically difficult, slow in operation and more error prone. In the second approach, since the data are dynamically read from RAM and written to RAM, operations are quite fast.

Figure 3.4 shows typical problem of a plate with a hole, subjected to uniaxial tension. Due to the symmetry of the problem one quarter of the plate could be considered for evaluation of the total fringe order. If the row-wise seeding and column-wise scanning is used, fringe order in the complete domain will be successfully unwrapped only if the primary seed point lies in the zone 1 of the Fig 3.4a. Conversely if column-wise seeding and row-wise scanning is used, primary seed point should lie in the zone 1 of Fig. 3.4b. If this is done phase map will be properly unwrapped.

If for some practical reasons, it is not possible to locate the primary seed point in these zones, viz. seed point is selected in zone 1 of Fig. 3.4a and row-wise seeding is used. Since in zone 1, width of model is smaller than in zone 2, this would lead to limited seeding only up to left boundary and secondary seed value for vertical scanning will be unreliable outside the boundary. Similarly, if primary seed point in Fig. 3.4b is selected in zone 2 with column-wise seeding and row-wise scanning then secondary seeding will be limited only up to lower boundary of zone 2 and problem of limited seeding arises again.

In such cases use of tiling could help in unwrapping the complete domain effectively. For row-wise seeding and column wise scanning if the primary seed point is in zone 2, then, the tiles needed for unwrapping are shown in Fig. 3.4c. Tile 1 will be unwrapped first based on primary seed value specified at point 'A', followed by row-wise seeding and column-wise scanning in zone 2, with primary seed value specified at any point on juncture of tiles. Since tile 1 is already unwrapped seed point for tile 2 can easily be located at any point on the common boundary of tile 1 and tile 2. Similarly for column wise seeding and row-wise scanning the tiles needed are shown in Fig. 3.4d.

Besides this, the use of tiling avoids error propagation due to noise, e.g. if phase map contains noise in some zones and scanning crosses these zones. The error due to noise of these zones will propagate and unwrapped fringe orders become unreliable. On the other hand, if tiling is used, then the tiles can be arranged so that in no case the scanning is continued after noisy zones. In such cases, the good zone of phase map will be unwrapped separately as another tile and seed value for this tile will be independently supplied.

A software has been developed implementing these ideas and it supports the use of separate unwrapping threshold value for different tiles. User can

interactively supply threshold value, along with the seed point in each of the tiles. The software supports both, row-wise seeding with column-wise scanning and column-wise seeding with row-wise scanning. Any of these two can be interactively used depending on the location of particular tile. The user has to make the tiling plan through menu selection and the tiles selected are internally stored in a tiling information file named *tile.dat*.

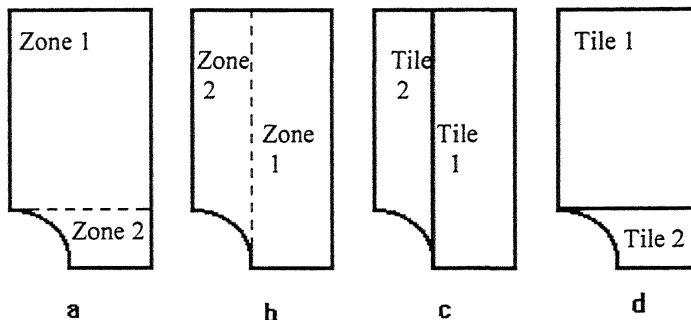


**Fig. 3.4.** Tiling for phase unwrapping. Identification of zones for locating the primary seed point: a row-wise seeding and column-wise scanning b column-wise seeding and row-wise scanning. Tiles required for c row-wise seeding and column-wise scanning d column-wise seeding and row-wise scanning.

Some general guidelines for proper selection of tiles are discussed in subsequent topics through the problems of disk and ring under diametral compression, rail road contact and spanner tightening the nut.

### 3.6 Tiles for Problem of Disk

Due to symmetry of model the discussion is restricted to one quarter of the image. As in this problem supplying the primary seed point along the horizontal or vertical diameter is not a problem, so the use of tiling does not serve any major purpose. If due to some problems, viz. presence of noise in phase map along these diameters, it is not possible to select a seed point along these diameters then any of the tiling arrangements shown in 2<sup>nd</sup>, 3<sup>rd</sup> or 4<sup>th</sup> quadrant (Fig. 3.5a) can be used to effectively unwrap the phase map.

In practice, the tiles chosen can overlap. In order to test the implementation of the software, tiling plans used for the problem of disk under diametral compression are shown in Fig. 3.5b, 3.5c and 3.5d. Tables 3.2-3.4 give the corresponding unwrapping parameters. The phase map is shown in Fig. 3.5e. Figure 3.5f shows the location of points for which sample data of unwrapped fringe orders are collected for comparison. These points correspond to points noted in Table 3.5.

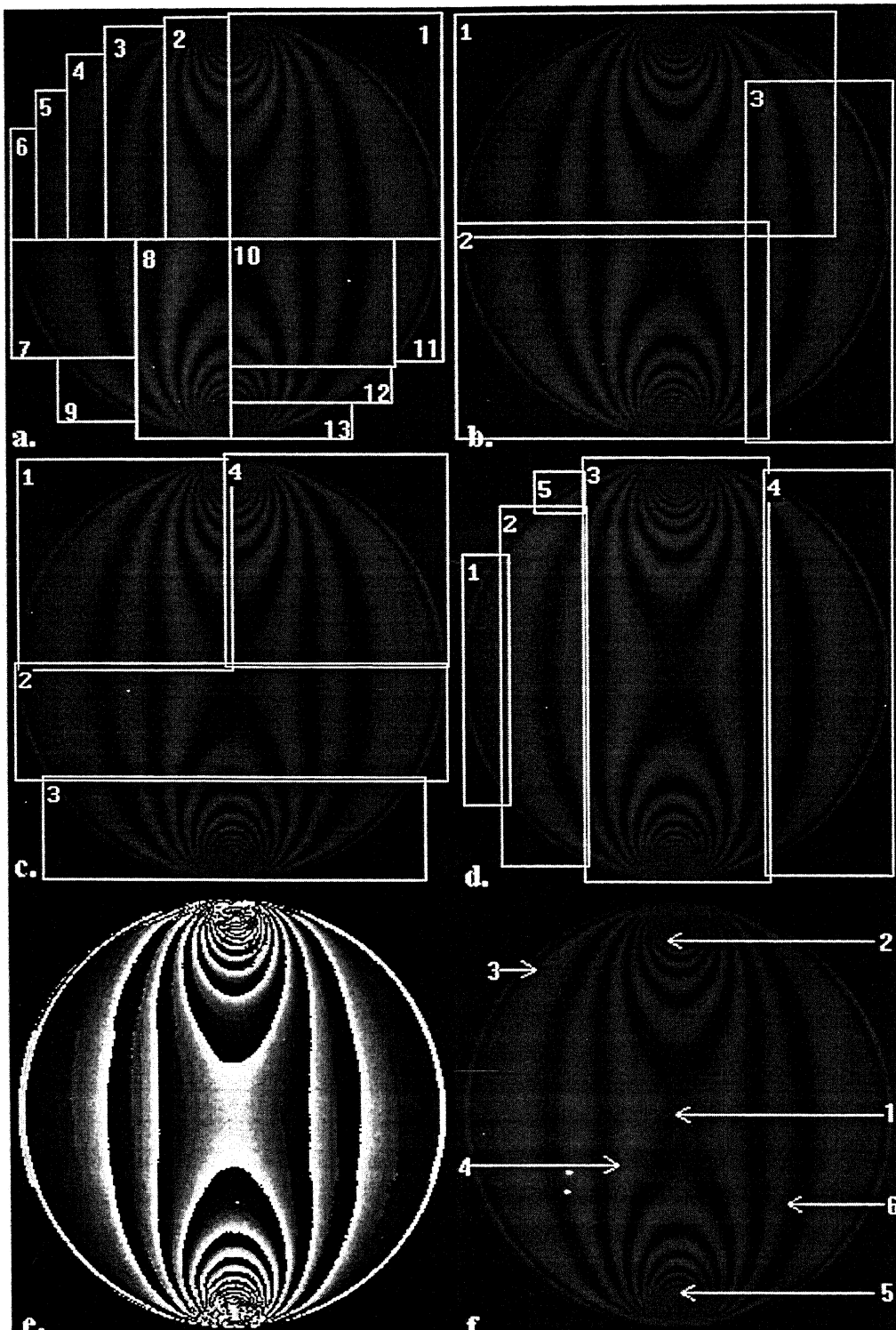


Fig. 3.5. a Some tiling arrangements for the problem of disk under diametral compression b,c,d Tiles used for unwrapping corresponding to Table 3.2-3.4 e Phase map used for unwrapping f Sample data points marked on the dark field image corresponding to Table 3.5.

**Table 3.1** Unwrapping parameters used for unwrapping complete image for problem of disk

Tile	Tile Coordinates	Seed Point	Seed Value (N)	Threshold (tp)	Seeding
1	(0,0) (511,511)	(256,170)	2.00	140	Row-wise

**Table 3.2** Unwrapping parameters and tiling plan 1 for problem of disk

Tile	Tile Coordinates	Seed Point	Seed Value (N)	Threshold (tp)	Seeding
1	(7,9) (442,267)	(343,251)	2.00	140	Row-wise
2	(6,251) (367,501)	(170,262)	2.00	140	Row-wise
3	(340,88) (506,504)	(402,263)	1.00	140	Row-wise

**Table 3.3** Unwrapping parameters and tiling plan 2 for problem of disk

Tile	Tile Coordinates	Seed Point	Seed Value (N)	Threshold (tp)	Seeding
1	(13,13) (259,257)	(170,246)	2.00	140	Row-wise
2	(8,248) (504,385)	(111,254)	1.00	140	Row-wise
3	(41,380) (479,498)	(128,386)	1.00	140	Row-wise
4	(251,7) (507,253)	(305,143)	3.00	140	Column-wise

**Table 3.4** Unwrapping parameters and tiling plan 3 for problem of disk

Tile	Tile Coordinates	Seed Point	Seed Value (N)	Threshold (tp)	Seeding
1	(12,122) (67,413)	(17,253)	0.00	140	Row-wise
2	(57,67) (157,483)	(111,255)	1.00	140	Row-wise
3	(152,11) (366,500)	(170,257)	2.00	140	Row-wise
4	(360,24) (506,492)	(402,254)	1.00	140	Row-wise
5	(96,26) (154,75)	(151,71)	1.00	140	Row-wise

Three dimensional plots of the unwrapped fringe order for each of the arrangements of Table 3.1-3.4 are shown in Fig. 3.6a, 3.6b, 3.6c and 3.6d respectively. It can be seen that fringe order plots are not sharp near the point of application of load at upper end. This is because in that zone phase map contains noise. Also, in second tiling arrangement unwrapping in that zone is very bad and gives negative fringe orders. This is because the column-wise seeding used for that tile crosses noise in phase map. Thus secondary seeding is completely disturbed due to noise and subsequent row-wise scanning loses its significance. This indicates, that the bad choice of seeding and scanning directions can adversely affect the results. The results summarized in Table 3.5 indicate the success in implementing tiling concept for phase unwrapping.

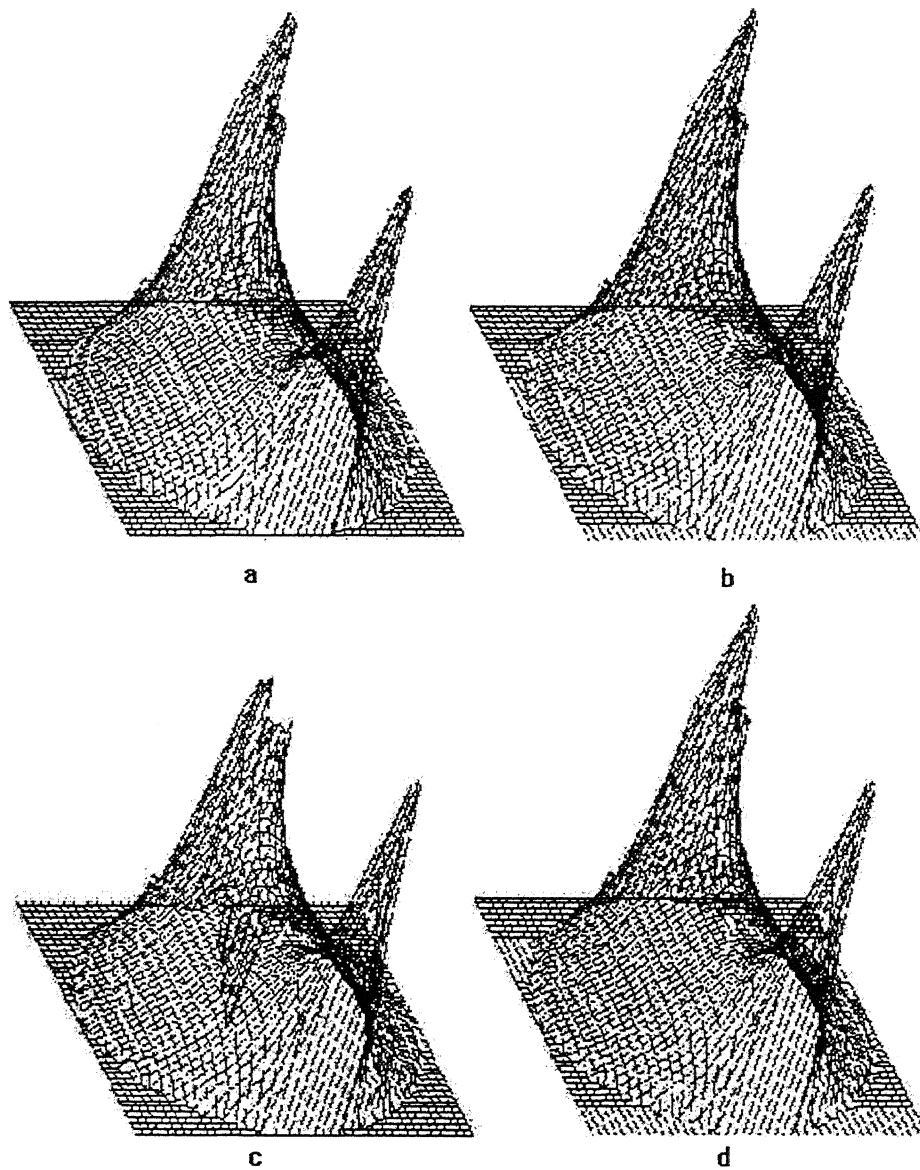


**Fig. 3.6** Three dimensional plots for fringe orders unwrapped with different tiling arrangements shown in Tables 3.1-3.4 respectively

**Table 3.5** Fringe orders at some salient points unwrapped with different tiling arrangements shown in tables 3.1-3.4

No.	Coordinates	Unwrapped Fringe Order (N)			
		Without Tiling	1	2	3
1	(256,256)	2.82	2.91	2.92	2.92
2	(248,57)	7.19	7.25	7.28	7.28
3	(93,91)	0.21	0.31	0.31	0.31
4	(187,315)	2.28	2.37	2.38	2.38
5	(260,461)	9.13	9.22	9.21	9.22
6	(384,358)	1.13	1.23	1.22	1.22

### 3.7 Tiles for Problem of Annular Ring

A few tiling arrangements for the problem of the annular ring under diametral compression is shown in Fig. 3.7a. It can be noted that the tiling arrangement is so chosen, that either of the row-wise or column wise seeding in each of tile will serve the purpose, if the primary seed point is selected properly. Since for all practical purposes it is difficult to judge the total fringe order in tiles 3 and 5, the unwrapping procedure should be started from any one of the 1<sup>st</sup>, 2<sup>nd</sup>, 4<sup>th</sup> or 6<sup>th</sup> tile and then be extended to 3<sup>rd</sup> and 5<sup>th</sup> tiles. The tiles can be made overlapping to each other to further simplify the selection of seed points in subsequent tiles.

Tables 3.6 to 3.8 show the different tiling arrangements and unwrapping parameters used to unwrap the phase map of Fig. 3.7d for the problem of annular ring under diametral compression with  $512 \times 512$  image size. Corresponding tiles are shown in Fig. 3.7b and 3.7c respectively. Table 3.9 shows the unwrapped fringe orders at some salient points for each of these tiling arrangements. These sample points are marked on the phase map in Fig. 3.7e. Figure 3.8a shows the three dimensional plot for fringe order data for ring, generated theoretically. Three dimensional plots of the unwrapped fringe order for each of the tiling arrangements of Tables 3.6-3.8 are shown in Fig. 3.8b, 3.8c and 3.8d respectively.

**Table 3.6** Unwrapping parameters used for unwrapping complete image for problem of ring

Tile	Tile Coordinates	Seed Point	Seed Value (N)	Threshold (tp)	Seeding
1	(0,0) (511,511)	(372,111)	3.00	140	Row-wise

**Table 3.7** Unwrapping parameters and tiling plan 1 for problem of ring

Tile	Tile Coordinates	Seed Point	Seed Value (N)	Threshold (tp)	Seeding
1	(45,16) (470,139)	(376,119)	3.00	140	Row-wise
2	(45,375) (467,495)	(403,387)	2.00	140	Row-wise
3	(11,139) (136,375)	(123,185)	3.00	140	Row-wise
4	(378,139) (502,375)	(412,357)	2.00	140	Column-wise
5	(136,139) (256,256)	(170,145)	3.00	140	Row-wise
6	(256,256) (378,375)	(338,368)	3.00	140	Row-wise
7	(136,256) (256,375)	(178,371)	3.00	140	Row-wise
8	(256,139) (378,256)	(377,166)	3.00	140	Column-wise

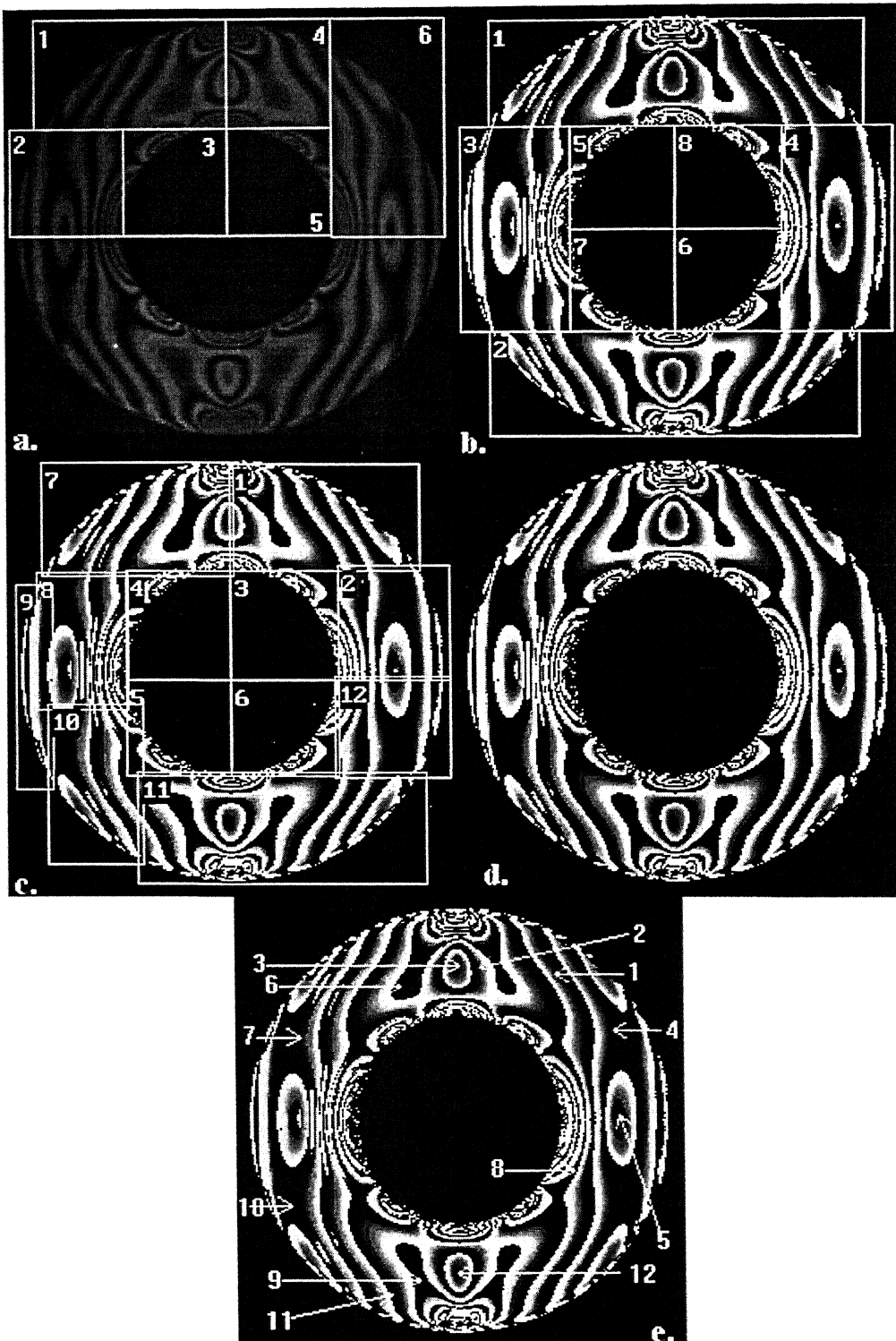


**Fig. 3.7.** a Some tiling arrangements for the problem of ring under diametral compression b,c Tiles used for unwrapping corresponding to Table 3.7-3.8 d Phase map used for unwrapping e Sample data points marked on the phase map corresponding to Table 3.9.

**Table 3.8** Unwrapping parameters and tiling plan 2 for problem of ring

Tile	Tile Coordinates	Seed Point	Seed Value (N)	Threshold (tp)	Seeding
1	(254,17) (470,138)	(379,125)	3.00	140	Row-wise
2	(376,132) (505,264)	(411,210)	2.00	140	Row-wise
3	(254,138) (376,254)	(341,144)	3.00	140	Row-wise
4	(136,138) (254,264)	(151,162)	3.00	140	Column-wise
5	(136,264) (254,374)	(175,369)	3.00	140	Row-wise
6	(254,264) (376,374)	(336,369)	3.00	140	Row-wise
7	(40,15) (259,144)	(134,116)	3.00	140	Row-wise
8	(35,141) (138,298)	(95,175)	2.00	140	Row-wise
9	(10,155) (52,390)	(47,258)	1.00	140	Row-wise
10	(46,293) (155,477)	(129,341)	3.00	140	Row-wise
11	(148,370) (476,498)	(372,396)	3.00	140	Row-wise
12	(372,260) (504,377)	(413,315)	2.00	140	Row-wise

**Table 3.9** Fringe orders at some salient points unwrapped with different tiling arrangements shown in Tables 3.6-3.8

No.	Coordinates	Unwrapped Fringe Order (N)		
		Without Tiling	1	2
1.	(369,87)	2.62	2.62	2.62
2.	(281,80)	3.63	3.63	3.62
3.	(255,79)	2.43	2.43	2.49
4.	(433,153)	1.30	1.30	1.30
5.	(440,248)	0.11	0.12	0.11
6.	(187,102)	4.08	4.08	4.15
7.	(73,160)	1.18	1.25	1.22
8.	(388,312)	<b>4.09</b>	3.10	3.11
9.	(207,437)	<b>3.08</b>	4.08	4.09
10.	(62,352)	<b>0.07</b>	1.18	1.16
11.	(176,452)	<b>4.10</b>	3.10	3.11
12.	(252,428)	<b>1.43</b>	2.43	2.44

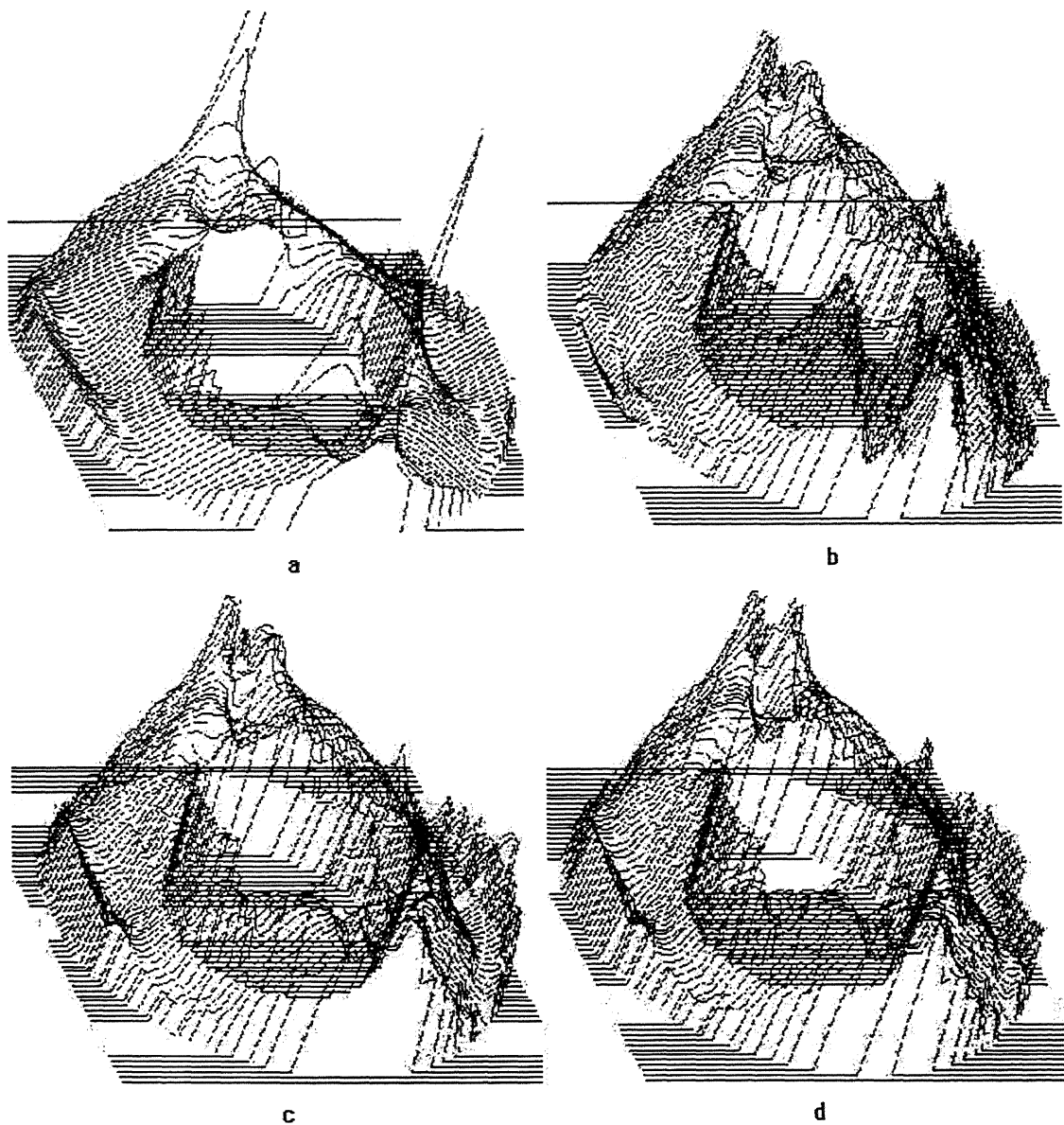


**Fig. 3.8** Three dimensional fringe order plots: a Theoretical data for ring b,c,d phase map of Fig. 3.7d unwrapped with different tiling arrangements shown in Tables 3.6-3.8 respectively

Note that for points 8-12 unwrapped fringe order with complete image are not matching back to corresponding phase map and are shown bold. Since magnitude of error is almost one complete fringe order, it can be because of some noise pixel causing propagation of error to these zones. These fringe orders are improved after use of tiling as shown in 2<sup>nd</sup> and 3<sup>rd</sup> tiling plan fringe order column.

### 3.8 Tiling Applied to Rail Road Contact Problem

Tiling arrangement for the left half of the model is shown in Fig. 3.9a. Here, all tiles can be merged into a single large tile as long as it is possible to give primary seed point in the zone 2 followed by row-wise seeding and column-wise scanning. Otherwise one should go for tiling. It is interesting to note that, if 4<sup>th</sup> and 5<sup>th</sup> tiles are merged and seed point is given at top or bottom boundary and row-wise seeding is done, the concave boundary of the model will be encountered twice in some of the vertical scans. This will create problem as the phase information outside the model will be unreliable and error will propagate. So it is better to keep 4<sup>th</sup> and 5<sup>th</sup> tile as two separate tiles.

Tables 3.10 to 3.12 show the different tiling arrangements and corresponding unwrapping parameters used to unwrap the phase map of Fig. 3.9d for the rail road contact problem with 512×512 image size. Corresponding tiles on the dark field image are shown in Fig. 3.9b and 3.9c. Table 3.13 shows the unwrapped fringe orders at some salient points for each of these tiling arrangements. These points are marked on corresponding dark field image and shown in Fig. 3.9e. Three dimensional plots of the unwrapped fringe order for each of the tiling arrangements of tables 3.10-3.12 are shown in Fig. 3.10a, 3.10b and 3.10c respectively.

**Table 3.10** Unwrapping parameters used for unwrapping complete image for rail road contact problem

Tile	Tile Coordinates	Seed Point	Seed Value (N)	Threshold (tp)	Seeding
1.	(0,0) (511,511)	(111,231)	1.00	140	Row-wise

**Table 3.11** Unwrapping parameters and tiling plan 1 for phase unwrapping of rail road contact problem

Tile	Tile Coordinates	Seed Point	Seed Value (N)	Threshold (tp)	Seeding
1.	(32,211) (483,329)	(160,246)	2.00	140	Row-wise
2.	(44,82) (491,222)	(108,184)	1.00	140	Row-wise
3.	(259,324) (391,437)	(294,396)	3.00	120	Column-wise
4.	(118,326) (263,441)	(220,335)	3.00	120	Row-wise
5.	(197,437) (307,511)	(252,501)	3.00	120	Row-wise

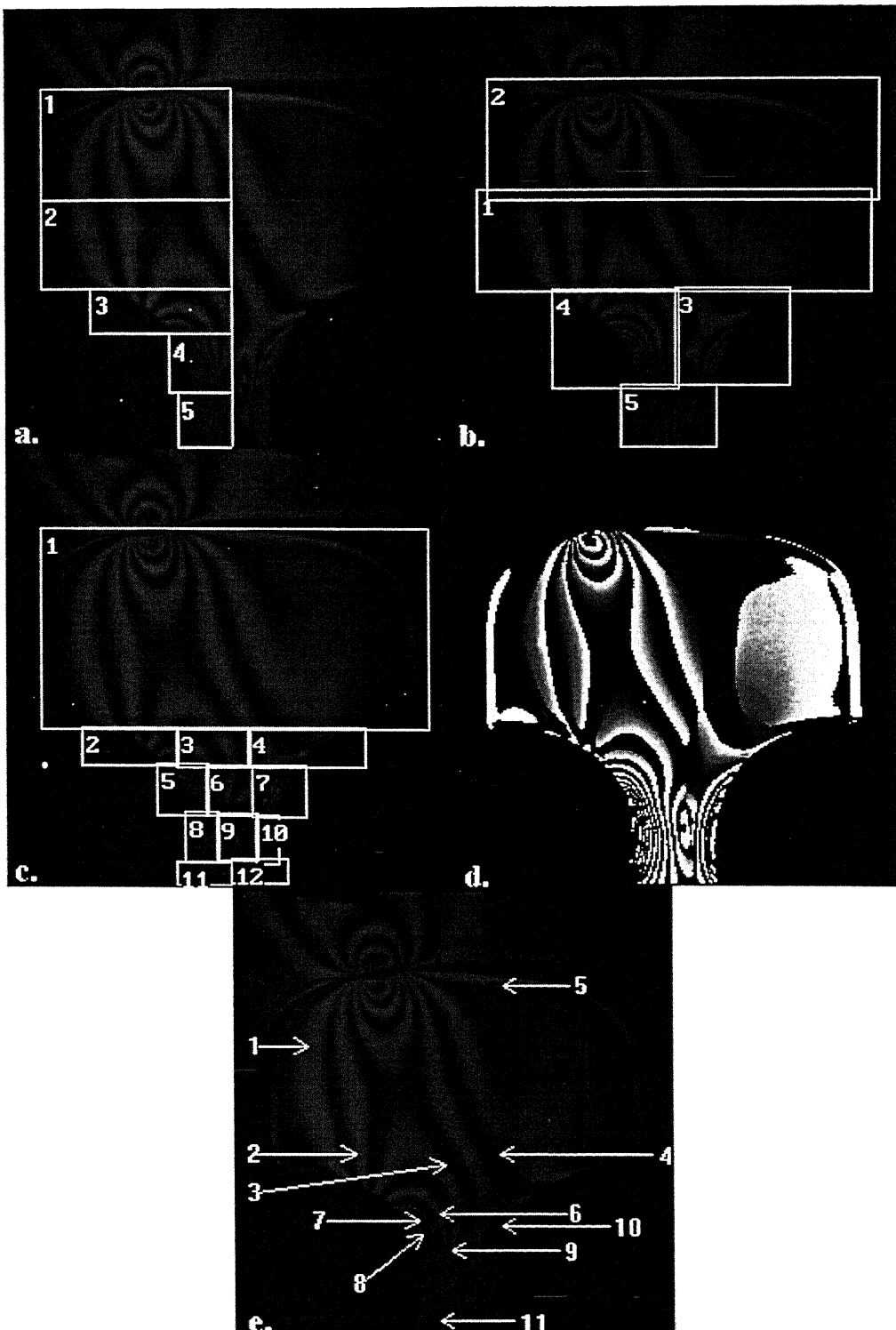


**Fig. 3.9.** a Some tiling arrangements for the rail road contact problem b,c Tiles used for unwrapping corresponding to Table 3.10-3.12 d Phase map used for unwrapping e Sample data points marked on the dark field image corresponding to Table 3.13.

**Table 3.12** Unwrapping parameters and tiling plan 2 for phase unwrapping of rail road contact problem

Tile	Tile Coordinates	Seed Point	Seed Value (N)	Threshold (tp)	Seeding
1.	(40,94) (484,326)	(159,236)	2.00	140	Row-wise
2.	(87,324) (196,368)	(188,334)	3.00	140	Row-wise
3.	(195,324) (278,370)	(240,359)	3.00	140	Column-wise
4.	(276,324) (410,370)	(327,368)	3.00	140	Row-wise
5.	(172,366) (231,426)	(221,371)	4.00	140	Row-wise
6.	(229,369) (281,426)	(245,374)	3.00	140	Row-wise
7.	(280,368) (342,429)	(293,398)	3.00	140	Row-wise
8.	(205,423) (242,481)	(232,472)	6.00	120	Row-wise
9.	(240,424) (287,479)	(252,477)	3.00	140	Row-wise
10.	(284,427) (310,482)	(289,475)	4.00	120	Row-wise
11.	(194,480) (257,506)	(239,501)	4.00	120	Row-wise
12	(256,477) (321,505)	(284,500)	3.00	120	Row-wise

**Table 3.13** Fringe orders at some salient points for the rail road contact problem unwrapped with different tiling arrangements shown in Tables 3.10-3.12

No.	Coordinates	Unwrapped Fringe Order (N)		
		Without Tiling	1	2
1.	(86,180)	0.38	0.38	0.39
2.	(140,304)	1.39	1.40	1.40
3.	(244,315)	2.20	2.21	2.21
4.	(308,304)	<b>0.18</b>	<b>0.19</b>	<b>0.19</b>
5.	(312,109)	0.20	0.21	0.22
6.	(237,372)	3.28	3.29	3.30
7.	(211,380)	<b>4.20</b>	<b>4.21</b>	<b>4.23</b>
8.	(215,396)	<b>4.10</b>	<b>4.10</b>	<b>4.13</b>
9.	(252,413)	<b>3.15</b>	<b>3.16</b>	<b>3.17</b>
10.	(309,387)	<b>-1.67</b>	<b>2.33</b>	3.33
11.	(238,494)	<b>3.10</b>	<b>3.12</b>	4.14

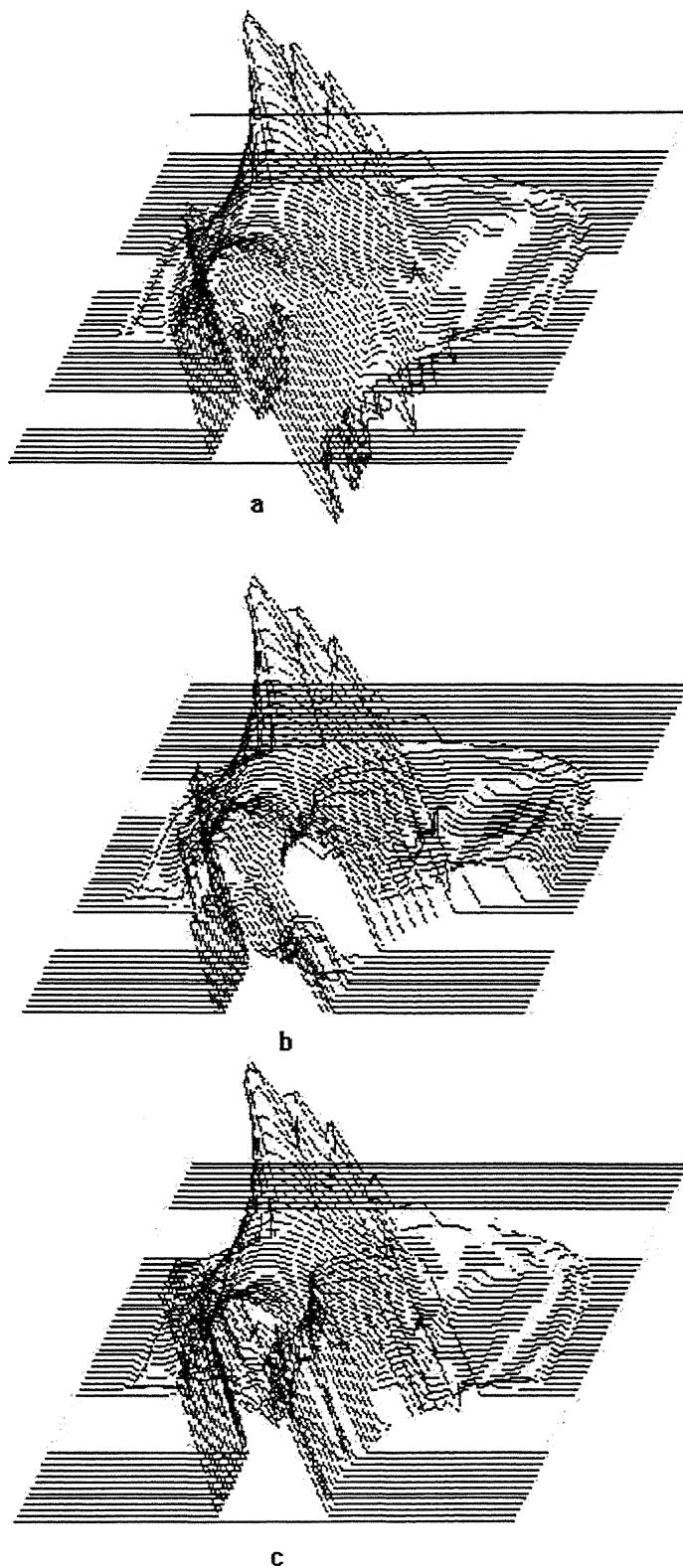


**Fig. 3.10** Three dimensional fringe order plots for phase map of rail road contact problem (Fig. 3.9d) unwrapped with different tiling arrangements shown in Tables 3.10-3.12 respectively

Note that unwrapped fringe orders at some of the points are not matching back to phase map. These fringe orders are shown bold. Even with the arrangement 1 these fringe orders are not improved. Only marginal improvement could be achieved by using arrangement 2. This is because phase map in these zones is not good and contains noise. Therefore, even with best possible tiling arrangement, if phase map contains noise and is not good, unwrapping will not be effective.

### 3.9 Tiling for Problem of Spanner and Nut

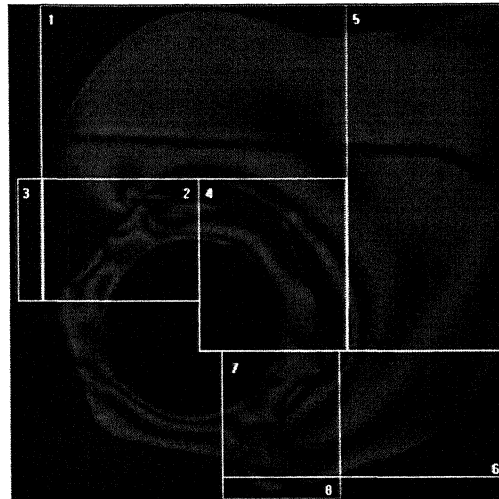


Fig. 3.11. Tiles for problem of spanner tightening the nut

Tiling arrangement for the problem of spanner and nut is shown in Fig. 3.11. It is clear that as the model geometry loses symmetry and becomes more and more complex, the freedom in selection of tiles is reduced and more skills are required for the proper selection of tiles. One of the other problem in phase unwrapping comes into picture here. Disturbance in the image due to loading fixture can be seen. During unwrapping in 1<sup>st</sup> and 5<sup>th</sup> tiles, this disturbance will propagate. Further, unwrapping procedure will completely be disturbed if the total fringe order at the seed points in neighboring tiles is supplied based on the results of 1<sup>st</sup> or 5<sup>th</sup> tile.

This requires a better selection of tiles for proper phase unwrapping. One of the other approach is shown in Fig. 3.12. Here tile 1 is divided in tiles 1 and 10. Also tile 5 is divided in tiles 5 and 9. Now unwrap tiles 1 and 5 separately. And for all other tiles start unwrapping procedure from tile 6 and proceed in the sequence 7-8-10-4-9-2-3 or so. Care must be taken in selecting primary seed points for tiles 9 and 10 and should not be based on results of tile 1 or 5 as they will be unreliable due to noise in phase map.

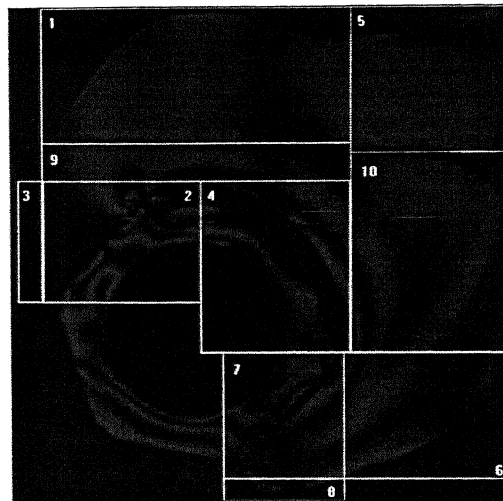


Fig. 3.12. Improved tiling arrangement for the problem of spanner tightening the nut

Phase maps for the problem of spanner tightening the nut is shown in Fig. 3.13. Because of complexity in model geometry as well as loading condition, stress field is very complex. Also, since exact behaviour of isoclinic data is not known *apriori*, phase map generation is quite involved. In such problems it is very difficult to identify the exact interface of phase reversal. Figure 3.13a shows phase map generated with six-step phase shifting images using  $\cos + \sin$  expression. Since the phase map generated by  $\cos + \sin$  expression is not good, interactive approach was used for phase map generation. Phase map generated with interactive approach is shown in Fig. 3.13b.

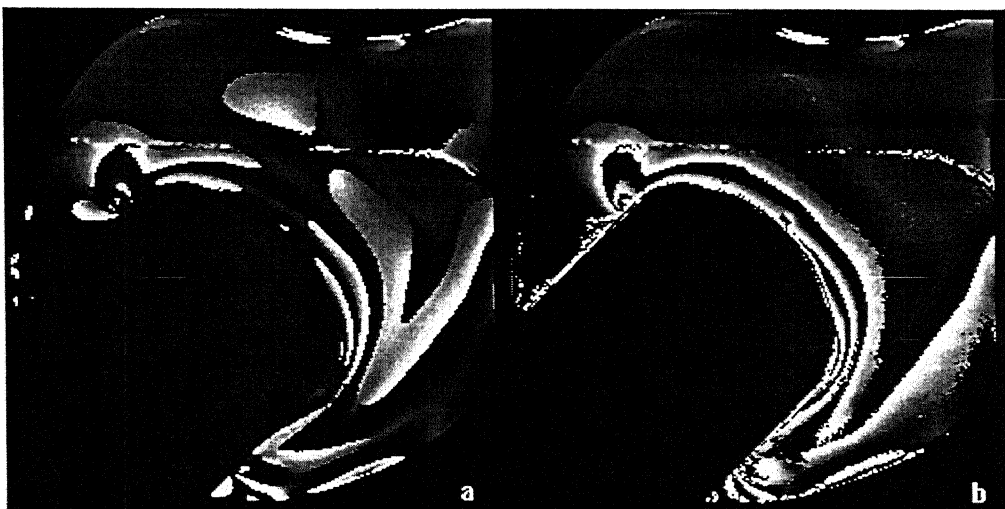


Fig. 3.13. Phase maps for Spanner problem: a Phase map obtained with  $\cos + \sin$  expression b Phase map obtained with interactive approach

Unwrapping parameters used for unwrapping complete image are shown in Table 3.14. Table 3.15 shows the different tile coordinates and corresponding unwrapping parameters used to unwrap the phase map of Fig. 3.13b for the problem of spanner and nut with  $512 \times 512$  image size. Corresponding tiles on a dark field image are shown in Fig. 3.14a. Table 3.16 shows the unwrapped fringe orders at some salient

points for each of unwrapping scheme. These points are shown, marked on a dark field image in Fig. 3.14b.

**Table 3.14** Unwrapping parameters used for unwrapping complete image for spanner and nut problem

Tile	Tile Coordinates	Seed Point	Seed Value (N)	Threshold (tp)	Seeding
1.	(0,0) (511,511)	(98,158)	1.00	140	Row-wise

**Table 3.15** Unwrapping parameters and tiling plan for phase unwrapping of spanner and nut problem

Tile	Tile Coordinates	Seed Point	Seed Value (N)	Threshold (tp)	Seeding
1.	(47,59) (129,262)	(101,154)	1.000	140	Row-wise
2.	(88,6) (311,146)	(96,119)	0.674	140	Row-wise
3.	(300,17) (498,148)	(306,100)	0.368	140	Row-wise
4.	(6,123) (73,315)	(64,160)	0.494	140	Row-wise
5.	(123,140) (336,199)	(127,163)	1.188	140	Row-wise
6.	(333,146) (497,207)	(361,148)	0.400	140	Row-wise
7.	(237,195) (394,29)	(295,198)	1.152	140	Row-wise
8.	(388,200) (499,300)	(432,207)	0.498	140	Row-wise
9.	(319,288) (49,380)	(343,290)	2.003	140	Row-wise
10.	(272,377) (495,446)	(342,400)	1.000	140	Row-wise
11.	(195,428) (294,507)	(248,489)	1.000	140	Row-wise
12	(290,442) (441,505)	(293,485)	2.345	140	Column-wise

**Table 3.16** Fringe orders at some salient points for the spanner and nut problem obtained by unwrapping with and without tiling.

No.	Coordinates	Unwrapped Fringe Order (N)	
		Without Tiling	With Tiling
1.	(123,159)	1.18	1.17
2.	(256,195)	1.90	1.89
3.	(56,174)	0.27	0.27
4.	(354,278)	1.30	1.29
5.	(120,190)	2.15	2.14
6.	(188,86)	0.40	0.39
7.	(267,87)	0.35	0.34
8.	(380,61)	0.34	0.33
9.	(405,40)	0.37	0.36
10.	(403,282)	0.15	0.14
11.	(426,279)	0.21	0.20
12.	(120,199)	2.95	2.94

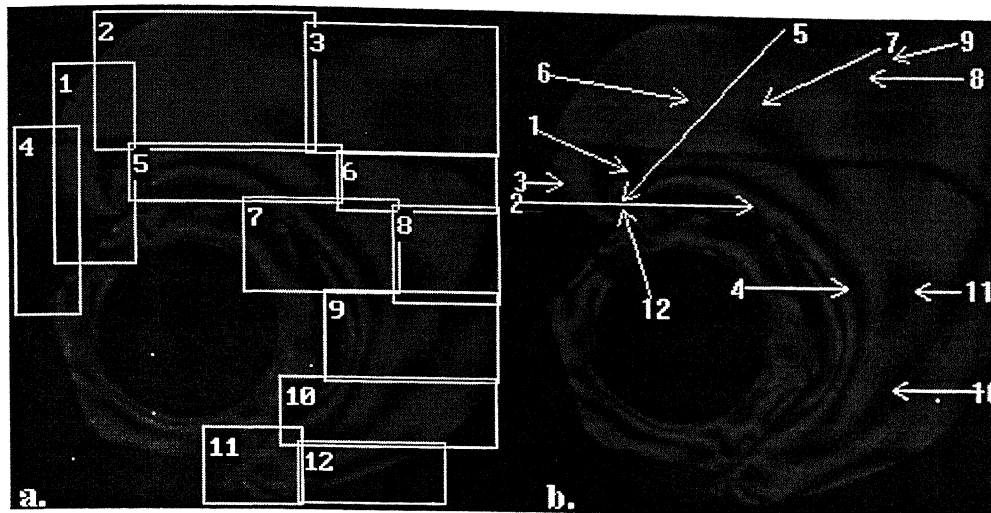


Fig. 3.14. Problem of Spanner and Nut a Tiles used for unwrapping corresponding to Table 3.15. b Sample points of Table 3.16 marked on the dark field image

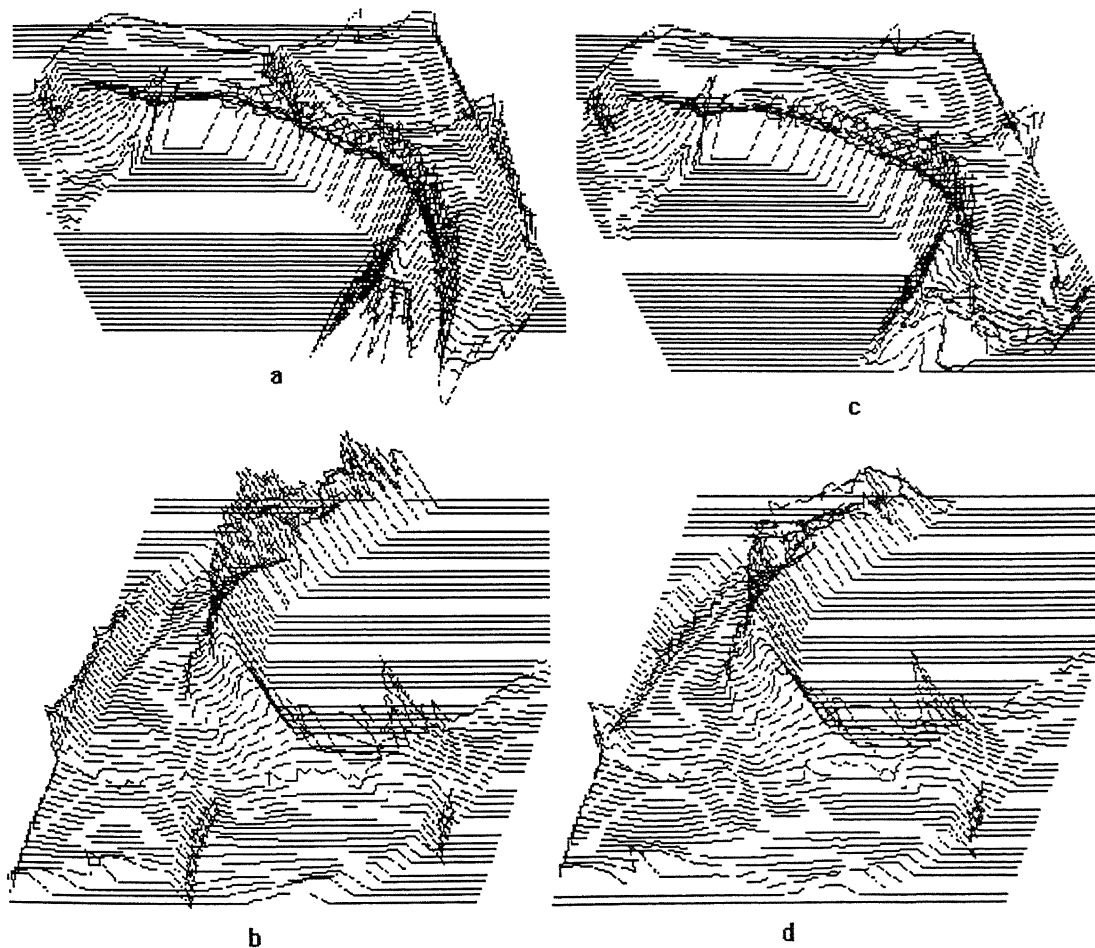


Fig. 3.15 Three dimensional fringe order plots for phase map of Fig. 3.14b for the problem of spanner tightening a nut. a Unwrapped without tiling (SW isometric) b Unwrapped without tiling (NW isometric) c Unwrapped with tiles shown in Table 3.15 (SW isometric) d NW isometric view of (c)

Figures 3.15a and 3.15b show the three dimensional plots of the unwrapped fringe order for unwrapping of complete image. Fringe orders unwrapped with scheme of Table 3.15 are shown in Fig. 3.15c and 3.15d.

As is clear from total fringe order plots, phase unwrapping is improved. Noise in phase map due to loading fixture has caused one kink in the upper portion of fringe order plot. This was effectively removed by the use of tiling.

### 3.10 Closure

From the above discussion it is clear that tiling procedure can be useful for a good number of practical unwrapping problems. Also this can help in unwrapping in high fringe gradient zones, as unwrapping threshold  $T_p$  can be selected lower for particular tile of high fringe gradient. Obviously the tiling concept calls for more user interaction. Error propagation due to noise can be prevented by proper selection of tiles.

Proper understanding of fringe order variation from dark and bright field images and identification of phase reversal interfaces is important for generation of correct phase map, as no tiling can provide good results in phase unwrapping if, phase map itself is not correct. Generated phase map should tally with corresponding dark and bright field images, if not, more refinement of phase map by interactive approach should be done [13].

Currently the software accepts only rectangular tiles. Integration of boundary identification routines with tile selection for accepting any generic tile shape can further reduce the calculational overheads.

# **STRESS SEPARATION USING SHEAR DIFFERENCE TECHNIQUE**

## **4.1 Introduction**

Photoelasticity provides two independent equations for 2-D problem and five independent equations for 3-D problem. Since there are three unknown stress components for 2-D and six unknown stress components for 3-D problem, the equations obtained are not sufficient to determine the complete state of stress at a point. Hence with a view to obtain additional relations, several auxiliary methods are required for both 2-D & 3-D problems, which in conjunction with photoelastic analysis can provide the complete information for solving a general stress problem.

Stress separation techniques, in a restricted sense, can be used to find the individual principal stresses and in a complete sense, they can provide all the components of the stress tensor. These methods can be either point-by-point or whole field. This is one of the most widely used methods in photoelasticity. However, it inherently bears the property of accumulation of errors. Tesar has modified the shear difference technique to minimize error accumulation [4]. The isoclinic parameter which is the chief source of error, is averaged along the three lines of grid and assumed to represent the isoclinic along the center line.

Correct determination of isoclinic parameters in the field of photoelasticity is still a challenging task. Since, correct determination of isoclinic parameter is the basic requirement for success of shear difference technique, application of median filter during isoclinic determination is discussed first.

## **4.2 Problems in Isoclinic Determination [7]**

The evaluation of isoclinic parameter is comparatively easier while determining it manually but the automated evaluation has several problems. The problems concerning the whole field isoclinic parameter evaluation can be roughly divided into the following parts,

1. Ambiguity in experimentally evaluating the isoclinic parameter.
2. Numerical inaccuracies.

It is to be noted that calculations for isoclinic calculation involve inverse trigonometric operations and thus one has a multi-valued solutions, this poses a problem of correctly evaluating the isoclinic parameter. In most of the equations the values returned by the arctangent functions are in the range of  $-\pi/4$  to  $+\pi/4$  only. In a model, *a priori* one does not know whether the fast or slow axis lies the range  $-\pi/4$  to  $+\pi/4$  and whether the isoclinic determined, corresponds to  $\sigma_1$  direction or  $\sigma_2$  direction. Thus the goal of isoclinic parameter evaluation should be such that it either gives  $\sigma_1$  or  $\sigma_2$  direction uniformly all over the domain. This problem could be solved [3] if theta is unwrapped in the range of  $-\pi/2$  to  $+\pi/2$ .

The problem of getting numerically correct value depends on the accurate recording and processing of the intensity information. In practical applications due to intensity digitization and quantization, only discrete values are used in the calculations. Also in the regions close to the isochromatic fringes, the error increases because of the ratios of small discrete values. Also there is a significant difference in the intensity maps of the images in theoretical and experimental conditions. These reasons lead to an error in the calculations.

### 4.3 Median Filtering in Isoclinic Calculation

Since shear difference is essentially a successive integration technique, a noise in either isochromatic or isoclinic parameter will disturb the integration procedure and successive results will loose their significance. Figures 4.1a and 4.1b show the isoclinic plot and theta field obtained by theoretically simulated images of disk under diametral compression for Brown and Sullivan algorithm. It can be seen that for all points where isochromatic fringe passes, the isoclinic determined has noise and oscillations. Causing the theta determined near an isochromatic to be unreliable and is called isochromatic interaction in determination of isoclinic. This suggests the noise removal in isoclinic determination.

For noise removal in isoclinic, first the theta field is plotted as an intensity map of theta value ranging from  $-\pi/4$  to  $+\pi/4$  over the 0-255 gray levels. Then noise present in the theta field is removed by the use of median filter. Now, the new intensity values are read from the image buffer, converted back to theta value and put in the file containing isoclinic data (\*.iso). Isoclinic plot and theta field obtained after application of above procedure on Fig. 4.1b are shown in Fig. 4.2a and 4.2b.

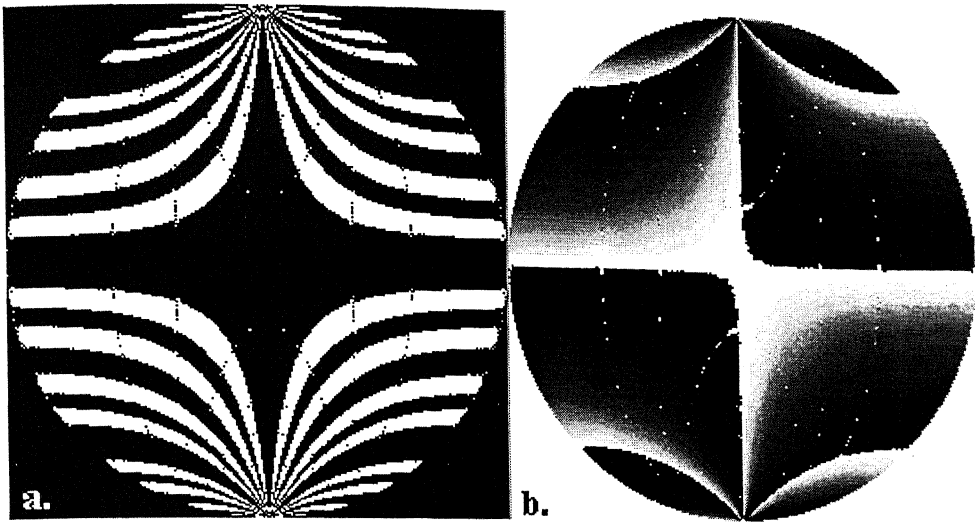


Fig. 4.1. a Isoclinic plot for the problem of disk under diametrical compression, obtained by application of Brown and Sullivan algorithm on theoretically simulated images b Corresponding theta field

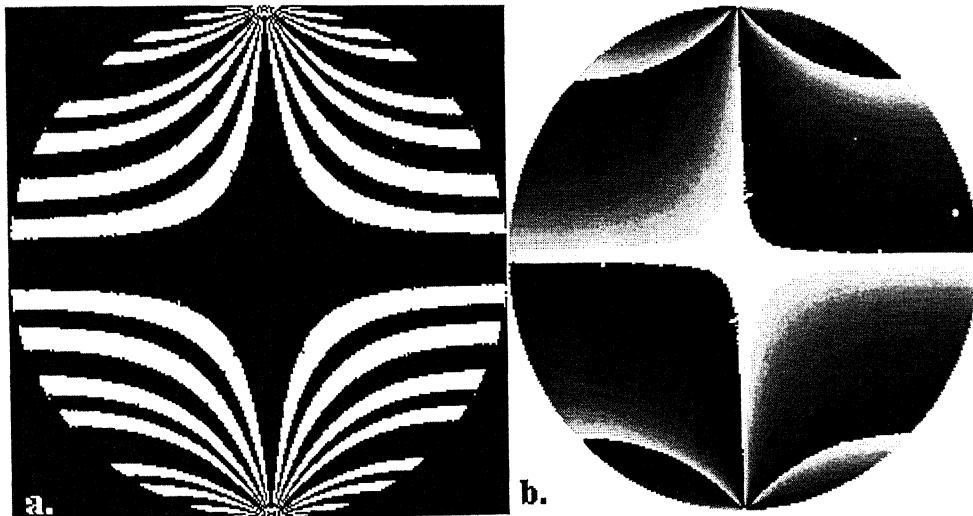


Fig. 4.2. Improved isoclinic data after application of median filter on Fig. 4.1b

However, for experimental images, interaction of isoclinic and isochromatic does not cause noise but produces oscillation in theta near an full order isochromatic. Isoclinic plot and theta field obtained with experimental images are shown in Fig. 4.3a and 4.3b. Thus the above median filtering technique serve no purpose in isoclinic improvement for experimental images as median filter can only remove *salt* and *pepper* noise. As reported by Vinayak [7] isoclinic determined will be more reliable if images are taken at low loads, i.e. isochromatic interaction is reduced. Figure 4.3a and 4.3b shows the isoclinic plot and theta field obtained by low load experimental images of Brown and Sullivan algorithm.

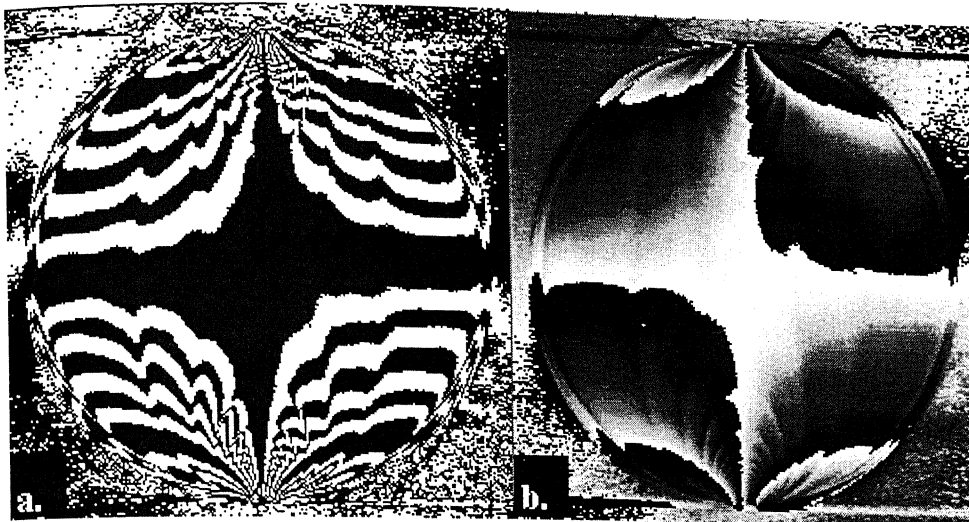


Fig. 4.3. a Isoclinic plot for the problem of disk under diametrical compression, obtained by application of Brown and Sullivan algorithm on experimental images b Corresponding theta field

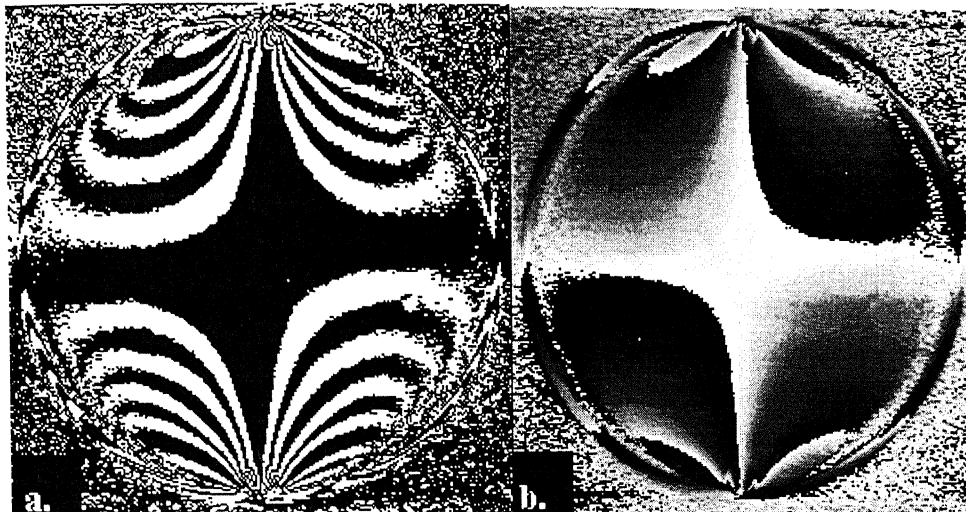


Fig. 4.4. a Isoclinic plot for the problem of disk under diametrical compression, obtained by application of Brown and Sullivan algorithm on Low Load experimental images b Corresponding theta field

It can be seen that theta determined with low load experimental images is better for the inner regions of model. But, near the boundary, due to interaction with zeroth fringe order, isoclinic determined are bad. Thus, a judicious combination of above two results can provide a reasonably accurate isoclinic value for further calculations of stress fields by shear difference technique, which is discussed in next section.

## 4.4 Shear Difference Technique for Stress Separation

### 4.4.1 Conventional Method

In the absence of body forces, the equation of equilibrium when applied to the problem of plane stress are,

$$\begin{aligned} \frac{\partial \sigma_x}{\partial x} + \frac{\partial \tau_{yx}}{\partial y} &= 0 \\ \frac{\partial \sigma_y}{\partial y} + \frac{\partial \tau_{xy}}{\partial x} &= 0 \end{aligned} \quad (4.1)$$

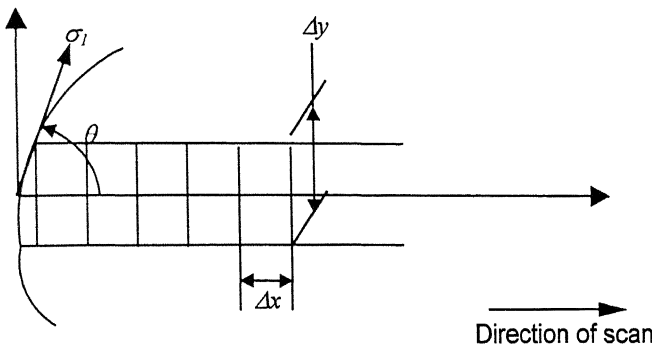


Fig. 4.5. Figure showing the grid needed for employing the shear difference method. The free boundary stress component is also shown.

In the shear difference method, one of the equations in Eq. (4.1) is integrated to separate the stresses. Thus one can do stress separation for lines parallel to  $x$ -axis or  $y$ -axis. If in a problem, the stresses have to be separated along lines parallel to  $x$ -axis, the first of Eq. (4.1) is integrated to become,

$$(\sigma_x)_j = (\sigma_x)_i - \int_i^j \frac{\partial \tau_{yx}}{\partial y} dx \quad (4.2)$$

Similarly for lines parallel to  $y$ -axis second of Eq. (4.1) leads

$$(\sigma_y)_j = (\sigma_y)_i - \int_i^j \frac{\partial \tau_{xy}}{\partial x} dy \quad (4.3)$$

Using the finite difference approximation, Eq. (4.2) can be rewritten as,

$$(\sigma_x)_j = (\sigma_x)_i - \sum_i^j \frac{\Delta \tau_{yx}}{\Delta y} \Delta x \quad (4.4)$$

where,  $(\sigma_x)_i$ ,  $(\sigma_y)_i$  are the stress value at the start of the integration procedure. If the starting point is chosen on a free boundary then  $(\sigma_x)_i$  is (if one has to do stress separation for lines parallel to  $x$ -axis)

$$(\sigma_x)_i = \sigma_1 \cos^2 \theta = \frac{N F_\sigma}{h} \cos^2 \theta \quad (4.5)$$

Once  $\sigma_x$  is calculated for a particular point on the grid,  $\sigma_y$  can be calculated as,

$$(\sigma_y)_i = (\sigma_x)_i - \frac{N F_\sigma}{h} \cos 2\theta \quad (4.6)$$

On similar lines, integration of the equilibrium equations can be done for the  $y$ -direction.

In above equations  $(\sigma_x)_i$ ,  $(\sigma_y)_i$  at the start of integration procedure chosen as boundary points where one of the component of stresses is zero. Thus isochromatic parameter at the boundary directly gives the value of the stress at the start of integration procedure.  $\tau_{xy}$  is then calculated at interior points and the summation proceeds in the stepwise manner using fixed grid with each block measuring  $\Delta x$  by  $\Delta y$ .  $\Delta \tau_{xy}$  is obtained from the difference between the top and bottom values at each interior points. In above equations the convention for positive  $x$  is from left to right while for positive  $y$  is from bottom to top. Here in present work the direction of the scanning is taken from left to right and right boundary is assumed to be straight vertical line. Equations derived above are also based on left to right scanning i.e. by standard convention.

The technique has come to be known as shear-difference technique because of the manner in which shear slope is calculated in Eq.(4.4) For performing the integration, one requires the data of both isochromatic and isoclinic fringe orders along the line of interest and for two more lines one above and the other below the line of interest.

One of the basic problems associated with the technique is that the numerical errors accumulate as one proceeds along the line of interest. Nevertheless, the technique has been quite widely used because of its simplicity.

#### 4.4.2 Improvement by Tesar [4]

One of the main sources of error accumulation in the conventional shear difference is the error in calculating the shear slope. It is well known that numerical differentiation is usually less accurate than numerical integration. Further, the calculation of the shear stress involves the use of isoclinic parameter whose measurement accuracy is generally poorer than that of the isochromatic fringe order. Tesar suggested that the shear stress be expressed in terms of the difference of principal stresses as,

$$\tau_{xy} = \frac{(\sigma_1 - \sigma_2)}{2} \sin 2\theta = \frac{N f_\sigma}{2h} \sin 2\theta \quad (4.7)$$

and be differentiated as a product of two functions. Substituting this into Eq. (4.2) gives,

$$(\sigma_x)_j = (\sigma_x)_i - \int_i^j \frac{\partial(\sigma_1 - \sigma_2)}{\partial y} \frac{1}{2} \sin 2\theta \, dx - \int_i^j (\sigma_1 - \sigma_2) \cos 2\theta \frac{\partial \theta}{\partial y} \, dx \quad (4.8)$$

Equation (4.8) can be approximated using the finite difference expressions as

$$(\sigma_x)_j = (\sigma_x)_i - \sum_i^j \frac{\Delta(\sigma_1 - \sigma_2)}{\Delta y} \frac{1}{2} \sin 2\theta \Delta x - \sum_i^j (\sigma_1 - \sigma_2) \cos 2\theta \frac{\Delta \theta}{\Delta y} \Delta x \quad (4.9)$$

The rest of the procedure is same as that of the conventional method.

## 4.5 Results and Discussion

Shear difference technique uses the isochromatic and isoclinic information for determination of normal stresses ( $\sigma_x$  and  $\sigma_y$ ) and shear stress ( $\tau_{xy}$ ). Thus for all reasons, success of shear difference technique depends on correct determination of these parameters.

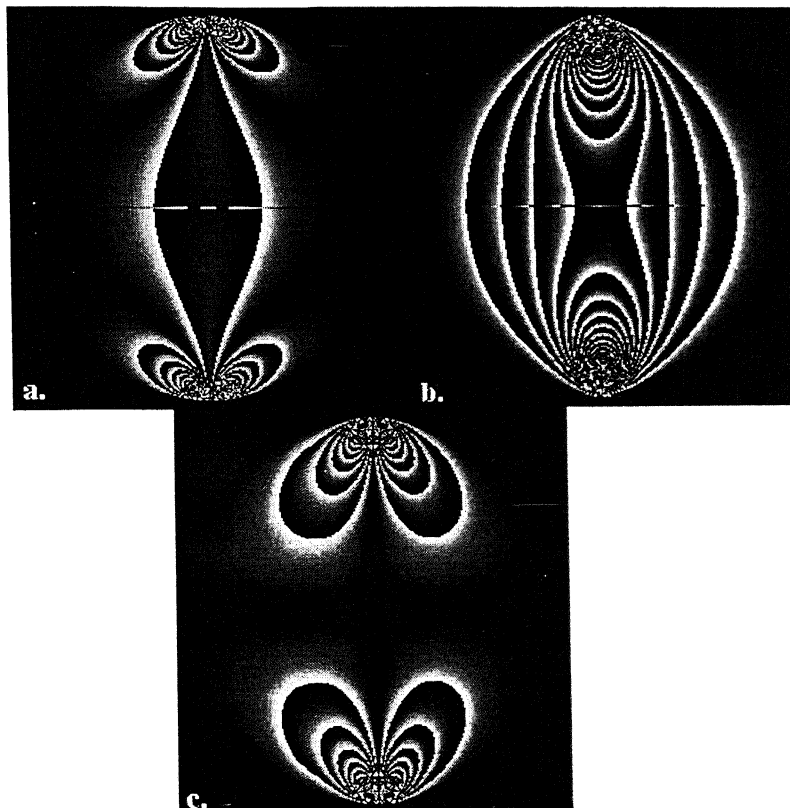


Fig. 4.6. Pseudo fringe contours showing variation of stresses, determined using theoretical data by Tesar's Modified Method a  $\sigma_x$  b  $\sigma_y$  c  $\tau_{xy}$

Theoretical contours of  $\sigma_x$ ,  $\sigma_y$  and  $\tau_{xy}$  for the problem of disk under diametral compression are shown in Fig. 4.6a, 4.6b and 4.6c respectively. These were obtained by first generating the isochromatic and isoclinic parameters theoretically, followed by the application of Tesar's modified stress separation technique on these data. Noise on the middle row is caused due to inaccurate generation of isoclinic data on that row. For stress separation, integration was carried out for each horizontal line from extreme left to extreme right.

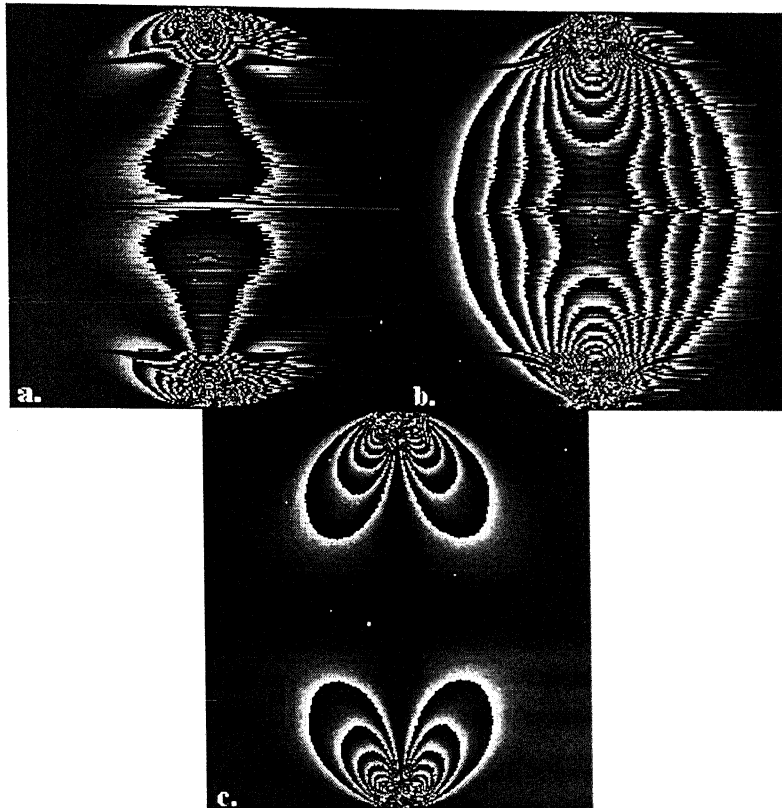


Fig. 4.7. Pseudo fringe contours showing variation of stresses, determined using data extracted from theoretically simulated images by Tesar's Modified Method a  $\sigma_x$  b  $\sigma_y$  c  $\tau_{xy}$

Figure 4.7 shows the separated stresses obtained by carrying out the actual calculations on theoretically simulated images. It can be seen that, even for the theoretically simulated images, stress contours does not match to the actual one. This is because, calculation of theta even from simulated images is not accurate. One can see that, for each row in the image  $\sigma_x$  and  $\sigma_y$  plots are good until the first isochromatic fringe is reached. Since theta calculated at this point is not accurate, separated stresses contain error. This error is accumulated in subsequent integration and stress plots afterwards are not good.

Comparison of above two case clearly indicates that error propagation due to numerical inaccuracies is negligible and main source of error in stress separation is inaccuracies in isoclinic calculations. This is further supported by the fact that, stress

contours obtained with data of simulated images show good match with theoretically calculated contours, till the first isochromatic in a row is crossed, i.e. first inaccuracy in theta.

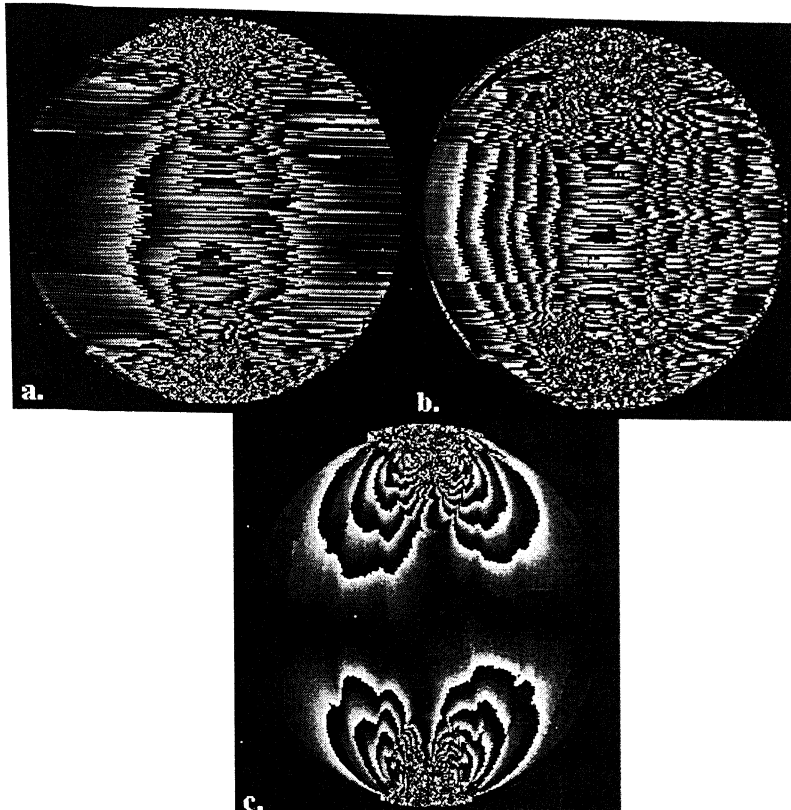


Fig. 4.8. Pseudo fringe contours showing variation of stresses, determined using data extracted from experimental images by Tesar's Modified Method a  $\sigma_x$  b  $\sigma_y$  c  $\tau_{xy}$

Separated stresses obtained with experimentally recorded images are shown in Fig. 4.8. Retardation calculation is carried out by six step phase shifting algorithm. Isoclinic parameters are calculated with Brown and Sullivan algorithm. These data were then put in a data file (\*.shd). Stress separation was carried out by Tesar's technique.

From the above two cases it can be seen that inaccuracies in calculation of isoclinic parameters does not affect the shear stress contours. This is because shear stresses are not determined by integration but is directly calculated for each point using isochromatic and isoclinic value at that point. Since at isochromatic fringes theta value become indeterminate, shear stress calculated at those points is also inaccurate, but they do not propagate.

## 4.6 Closure

Problems in isoclinic determination and some techniques for isoclinic improvement is discussed. Then stress separation technique was presented. Since it was observed that the chief source of error in stress separation is inaccurate determination of theta value, an accurate calculation of theta is required.

# **CONCLUSION AND SUGGESTIONS FOR FUTURE WORK**

## **5.1 Conclusion**

Unlike in conventional analysis, with advancement in digital photoelasticity data is available at pixel level. Thus the correct determination of fringe order values at each pixel in the domain is a crucial step. The main aim of this thesis is to develop an appropriate scheme, which will handle the phase map data efficiently for phase unwrapping, in the context of digital photoelasticity. The concept of tiling for effective phase unwrapping in the whole domain is presented. The applicability of the present scheme is verified for a variety of problems. The results of phase unwrapping are shown in the form of three dimensional fringe order plots.

Accurate evaluation of isoclinic parameter  $\theta$  is still a challenging task in the field of digital photoelasticity. The evaluation of isoclinic parameter  $\theta$  from the plane polariscope arrangement gives reasonably good results. Also isoclinic parameter obtained at low loads in circular polariscope arrangement is comparatively better. So these methods are recommended for future use. However, further refinement in isoclinic parameter evaluation should be the focus of future research.

## **4.2.Suggestion for Future Work**

1. Currently the software uses only rectangular tiles. This may be undesirable in certain class of problems due to complex geometry of the model. Use of boundary identification routines for generating tiles of any arbitrary shape can further improve the efficiency and effectiveness of phase unwrapping by tiling.
2. The software in Windows environment made for photoelastic analysis stores unwrapped fringe order data and isoclinic parameter in the form of a float value written directly to a file in text format. This puts memory overheads in storing these data. The use of binary file format to store these data can considerably reduce the memory required for storage of these data.
3. From results of in-plane shear stress  $\tau_{xy}$ , it can be seen that the isoclinic parameter does not have much effect on it. This tells that if some smoothening of  $\theta$  is done

before using it for stress separation, there is a higher probability of satisfactory results.

Since the isoclinic parameter  $\theta$ , plays an important role in the end results, there is a need for improvement of it.

# REFERENCE

Brown GM, Sullivan JL (1990) The computer-aided holophotoelastic method. *Exp Mech* 30(2):135-144

Mangal SK, Ramesh K (1999) Use of multiple loads to extract continuous isoclinic fringes by phase-shifting. *Strain* 35(1):15-17 Errata (1999). 35(2):76

Ramesh K, Digital Photoelasticity: Advanced Techniques and Application. Springer-Verlag, Berlin, Germany, 2000

Tesar V (1935) la photoelasticimetre et ses applications dans la construction aeronautique. *La Science Aerienne II*: 372-394

Ramesh K, Pathak PM (1988) Numerical techniques for stress separation in photoelasticity – a review. ARDB technical report. ARDB-SP-TR-919-01, India

Kulkarni AG, Stress Separation in Digital Photoelasticity by Shear Difference Technique. M.Tech thesis, Dept. of Mech. Engg. IIT Kanpur, 2000

Gadre VY, Evaluation of Isoclinic Parameter in Digital Photoelasticity. M.Tech thesis, Dept. of Mech. Engg. IIT Kanpur, 2000

Ramesh K, Ganeshan VR, Mullik SK (1991) Digital image processing of photoelastic fringes – a new approach. *Exp Tech* 15(5):41-46

Ramesh K, Pramod BR (1992) Digital image processing of fringe patterns in protomechanics. *Opt. Engg.* 31(7):1487-1498

Ramesh K, Singh RK (1995) Comparative performance evaluation of various fringe thinning algorithms in photomechanics. *J Electronic Imaging* 4(1):71-83

Patterson EA, Wang ZF (1991) Towards full field automated photoelastic analysis of complex components. *Strain* 27(2):49-56

Quiroga JA, González-Cano A (1997) Phase measuring algorithm for extraction of isochromatics of photoelastic fringe patterns. *Applied Optics* 36(32):8397-8402

Ramesh K, Mangal SK (2000) Phase-shifting calculations in 2D photoelasticity: revisited. *Aero. Society of India*, 0001-9267:121-136

Chen TY, Lin (1996) An improved method for whole field automatic measurement of principle stress direction. *Abst proc VIII International Conference on Experimental Mechanics*:178-179

Dupré JC, Bremand F, Lagarde A (1993) Photoelastic data processing through digital image processing: isostatics and isochromatics reconstruction. Presented at the Int Conference on Photoelasticity: New Instrumentation, Materials and Data Processing Techniques, London

Sarma VSSSR, Pillai SA, Subramanian G, Varadan TK (1992) Computerized image processing for whole-field determination of isoclinics and isochromatics. *Exp Mech* 32(1):24-29

Kihara T (1990) Automatic whole-field measurement of photoelasticity using linear polarized incident light. *Proc of IX Int Conference of Experimental Mechanics Copenhagen* 2:821-827

Ajovalasit A, Barone S, Petrucci G (1998) A method for reducing the influence of the quarter-wave plate error in phase shifting photoelasticity. *J Strain Analysis for Engg. Des.* 33(3):207-216

133624

33624

**Date Slip**

The book is to be returned on  
the date last stamped.



A133624